bioRxiv preprint doi: https://doi.org/10.1101/2022.04.26.489478; this version posted April 26, 2022. The copyright holder for this preprint (which was not certified by peer review) is the author/funder, who has granted bioRxiv a license to display the preprint in perpetuity. It is made available under aCC-BY 4.0 International license.

Shuffled ATG8 interacting motifs form an ancestral bridge between UFMylation and C53-mediated autophagy

Authors:

Lorenzo Picchianti[1,2*], Víctor Sánchez de Medina Hernández[1,2*], Ni Zhan[1*], Nicholas A. T. Irwin[3,7], Madlen Stephani[1,2], Harald Hornegger[4], Rebecca Beveridge[5], Justyna Sawa-Makarska[4], Thomas Lendl[6], Nenad Grujic[1], Sascha Martens[4], Thomas A. Richards[3], Tim Clausen[6], Silvia Ramundo[1], G. Elif Karagöz[4], Yasin Dagdas[1]

Affiliations

[1]Gregor Mendel Institute (GMI), Austrian Academy of Sciences, Vienna BioCenter (VBC), Vienna, Austria.
[2]Vienna BioCenter PhD Program, Doctoral School of the University of Vienna and Medical University of Vienna, A-1030, Vienna, Austria.
[3]Department of Zoology, University of Oxford, Oxford, UK
[4] Max Perutz Labs, Medical University of Vienna, Vienna BioCenter (VBC), Vienna, Austria.
[5]Department of Pure and Applied Chemistry, University of Strathclyde, Glasgow G1 1XL, Scotland
[6]Research Institute of Molecular Pathology (IMP), Vienna BioCenter (VBC), Vienna, Austria.
[7]Merton College, University of Oxford, Oxford, UK

*These authors contributed equally to this work

Correspondence: Elif Karagöz, guelsuen.karagoez@meduniwien.ac.at
Yasin Dagdas, yasin.dagdas@gmi.oeaw.ac.at

Abstract:

UFMylation mediates the covalent modification of substrate proteins with UFM1 (Ubiquitin-fold modifier 1) and regulates the selective degradation of endoplasmic reticulum (ER) via autophagy (ER-phagy) to maintain ER homeostasis. Specifically, collisions of the ER-bound ribosomes trigger ribosome UFMylation, which in turn activates C53-mediated autophagy that clears the toxic incomplete polypeptides. C53 has evolved non-canonical shuffled ATG8 interacting motifs (sAIMs) that are essential for ATG8 interaction and autophagy initiation. Why these non-canonical motifs were selected during evolution, instead of canonical ATG8 interacting motifs remains unknown. Here, using a phylogenomics approach, we show that UFMylation is conserved across the eukaryotes and secondarily lost in fungi and some other species. Further biochemical assays have confirmed those results and showed that the unicellular algae, *Chlamydomonas reinhardtii* has a functional UFMylation machinery, overturning the assumption that this process is linked to multicellularity. Our conservation analysis also revealed that UFM1 co-evolves with the sAIMs in C53, reflecting a functional link between UFM1 and the sAIMs. Using biochemical and structural approaches, we confirmed the interaction of UFM1 with the C53 sAIMs and found that UFM1 and ATG8 bound to the sAIMs in a different mode. Conversion of sAIMs into canonical AIMs prevented binding of UFM1 to C53, while strengthening ATG8 interaction. This led to the autoactivation of the C53 pathway and sensitized *Arabidopsis thaliana* to ER stress. Altogether, our findings reveal an ancestral toggle switch embodied in the sAIMs that regulates C53-mediated autophagy to maintain ER homeostasis.

bioRxiv preprint doi: https://doi.org/10.1101/2022.04.26.489478; this version posted April 26, 2022. The copyright holder for this preprint (which was not certified by peer review) is the author/funder, who has granted bioRxiv a license to display the preprint in perpetuity. It is made available under aCC-BY 4.0 International license.

Introduction

Perturbations of cellular homeostasis, termed "cellular stress", triggers protein aggregation and impairment of organelle function, and reduces organismal fitness and lifespan. Quality control pathways closely monitor the health of cellular components to alleviate cellular stress [1]. Cells first try to rescue aberrant proteins and organelles to restore cellular homeostasis [2–4]. If these attempts fail, dysfunctional proteins and organelles are rapidly degraded [5]. Defects in cellular quality control has been linked to several diseases, including cognitive decline, aging, cancer, and metabolic disorders in humans, and reduced stress tolerance and fitness in plants [1, 6–8]. Although, studies in the last decade have revealed a comprehensive suite of interconnected pathways that mediate protein and organelle degradation, the regulatory mechanisms that keep them switched off under normal conditions remain largely unknown.

Selective autophagy is a major quality control pathway that degrades unwanted or harmful cellular components including protein aggregates or damaged organelles with high precision [9]. Modular selective autophagy receptors (SARs) bring those cargo to the core autophagy machinery, resulting in their selective degradation [8, 10]. SARs recruit the autophagy machinery through their interaction with ATG8, a ubiquitin-like protein conjugated to the phagophore, and ATG11/FIP200, a scaffold protein of the autophagy initiation complex ATG1/ULK1 [11]. Recent structure-function studies have shown that SARs interact with ATG8 via various amino acid sequence motifs [4]. The **c**anonical **A**TG8 **I**nteracting **M**otif, (**cAIM**), also known as an **L**C3 **I**nteracting **R**egion (**LIR**), is a well characterized short linear motif that interacts with ATG8 by forming a parallel β-sheet with the β-sheet 2 in ATG8 [12]. The cAIM is represented by the WXXL consensus sequence, where W is an aromatic residue (W/F/Y), L is a aliphatic hydrophobic residue (L/I/V), and X can be any residue [13]. Recently, we showed that the ER-phagy receptor C53 (CDK5RAP3 in humans) interacts with plant and mammalian ATG8 isoforms via a non-canonical AIM sequence, with the consensus sequence IDWG/D, which we named the shuffled AIM (sAIM) [14]. However, the structural basis of sAIM-ATG8 interaction and its importance in C53-mediated autophagy and endoplasmic reticulum homeostasis remain unknown.

Our work and a recent genome wide CRISPR screen revealed that selective ER autophagy (ER-phagy) is regulated by UFMylation [14, 15]. UFMylation is similar to ubiquitination, where UFM1 is conjugated to substrate proteins via an enzymatic cascade [16, 17]. First, UFM1 is cleaved to its mature form by the protease UFSP2. UFM1 is then activated by UBA5, an E1 activating enzyme. UBA5 transfers UFM1 to UFC1, the E2 conjugating enzyme, through a trans-binding mechanism [18, 19]. Finally, UFM1 is transferred to the substrate by UFL1, which, in complex with the ER membrane protein DDRGK1, form an E3

bioRxiv preprint doi: https://doi.org/10.1101/2022.04.26.489478; this version posted April 26, 2022. The copyright holder for this preprint (which was not certified by peer review) is the author/funder, who has granted bioRxiv a license to display the preprint in perpetuity. It is made available under aCC-BY 4.0 International license.

37 ligase complex to covalently modify lysine residues on substrates [20, 21]. To date, the best
38 characterized UFMylation substrate is the 60S ribosomal subunit RPL26 [22]. RPL26
39 UFMylation is triggered by stalling of ER-bound ribosomes and is necessary for autophagic
40 degradation of the incomplete polypeptides trapped on ER-bound ribosomes [15, 23]. We
41 have shown that C53 mediates the degradation of these incomplete polypeptides in a
42 UFMylation-dependent manner [14]. However, how UFMylation regulates C53-mediated
43 autophagy remains unknown.
44
45 Here, we combined evolutionary analyses with cellular and structural biology experiments to
46 investigate the regulation of C53-mediated autophagy via UFMylation. We reconstructed the
47 evolutionary history of the UFMylation pathway and found that it is ubiquitous across
48 eukaryotes, suggesting its presence in the last eukaryotic common ancestor. Based on our
49 phylogenetic analyses, we reconstituted the UFMylation machinery of the unicellular green
50 algae, *Chlamydomonas reinhardtii*, and showed that it is functional and essential for the ER-
51 stress tolerance, demonstrating the importance of UFMylation beyond plants and animals.
52 Biochemical and structural studies, supported with evolutionary correlation analyses
53 revealed that shuffled AIMs (sAIMs) within C53 intrinsically disordered region (IDR) form
54 versatile binding sites that allow C53 to interact with both ubiquitin-like proteins (UBLs),
55 UFM1 and ATG8. However, ATG8 and UFM1 bind these motifs in a different mode. While
56 ATG8 bound strongest to cAIM and displayed equal preference for the first and the second
57 sAIM in C53 IDR, UFM1 interacted preferentially with the first sAIM. Conversion of sAIMs in
58 C53 into canonical AIMs shifted its binding preference towards ATG8 and led to premature
59 activation of autophagy driven by C53, sensitizing *Arabidopsis thaliana* to ER stress.
60 Altogether, our findings reveal an ancient UFM1 dependent regulatory mechanism that
61 prevents premature activation of C53-mediated autophagy.

62 ## Results

63 ### The UFMylation pathway is conserved across eukaryotes and functional in the
64 ### unicellular alga, *Chlamydomonas reinhardtii*

65 To explore a potential link between the UFMylation pathway and C53-mediated autophagy,
66 we searched for the existence of proteins involved in UFMylation across the eukaryotic tree
67 of life using a phylogenomic approach across 151 species. We identified the presence of
68 UFMylation proteins in all major eukaryotic lineages, indicating that the UFMylation pathway
69 was a feature of the last eukaryotic common ancestor (Fig. 1A, Fig. S1). Despite its
70 ancestral origin, multiple groups have lost parts or all the UFMylation proteins. Apparent
71 absence of a gene family can result from dataset incompleteness (e.g., incomplete genome
72 assembly and annotation) but recurrent absences across multiple closely related genomes is

bioRxiv preprint doi: https://doi.org/10.1101/2022.04.26.489478; this version posted April 26, 2022. The copyright holder for this preprint (which was not certified by peer review) is the author/funder, who has granted bioRxiv a license to display the preprint in perpetuity. It is made available under aCC-BY 4.0 International license.

73 strong evidence that a protein has been lost from those genomes and specific branches of
74 the tree of life. We noted the loss of UFMylation from multiple parasitic and algal lineages as
75 well as in fungi (Fig. 1A). Gene loss in parasites is a recurrent phenomenon, resulting from
76 parasitic genome streamlining [24], but the absence of UFMylation in genera such as
77 *Plasmodium*, *Entamoeba*, and *Trichomonas* indicates that the pathway is often expendable
78 in parasitic organisms (Fig. 1A). UFMylation has also been lost repeatedly in algal lineages,
79 suggesting that life history or other shared cellular characters may dictate the pathway's
80 retention. Similar to parasites and algae, fungi have also lost UFMylation, although certain
81 lineages retain pathway components, indicating that either repeated losses have occurred,
82 or genes were lost and subsequently reacquired through horizontal gene transfer (Fig. 1A).
83 Lastly, despite the loss of UFM1 in various lineages, certain UFMylation pathway proteins
84 are occasionally retained, particularly DDRGK1, UFL1, and in a few cases, C53 (e.g., the
85 oomycete genus *Albugo* and the chytrid class Neocallimastigomycetes) (Fig. 1A). This
86 suggests that these proteins may have additional cellular functions independent of UFM1.
87 Altogether, these data demonstrate that the UFMylation pathway is present throughout
88 eukaryotes, implying that it is functionally conserved in both unicellular and multicellular
89 species, unlike suggested before [22].
90
91 To characterize the functionality of the UFMylation pathway in a unicellular species, we
92 investigated UFMylation in *Chlamydomonas reinhardtii* (Cr), a single-celled green alga. We
93 purified CrUBA5, CrUFC1 and CrUFM1 and tested their ability to conjugate UFM1. *In vitro*
94 E2-charging of CrUFM1 worked similar to the human UFMylation cascade [18]. In a UBA5-
95 dependent manner, UFM1 was transferred to UFC1 by formation of a thioester bond, which
96 could be reduced by β-mercaptoethanol (Fig. 1B). This indicates that the UFM1 conjugation
97 mechanism is conserved in *C. reinhardtii*, prompting us to tested substrate UFMylation. We
98 first examined conservation of the RPL26 tail, which has been shown to be ufmylated [22].
99 Protein sequence alignment and Twincons analysis revealed that the ufmylated lysine
100 residues in RPL26 are conserved in species with UFM1, including *C. reinhardtii* (Fig. S2).
101 Moreover, immunoblot analysis using a UFM1 antibody revealed two bands corresponding
102 to mono- and di-ufmylated RPL26 (Fig. 1C). RPL26 UFMylation was dependent on the
103 UFMylation machinery, as both bands were absent in *uba5* and *ufl1* mutants (Fig. 1C, Fig.
104 S3). Consistent with previous studies [14, 23], RPL26 UFMylation was induced upon ER
105 stress triggered by tunicamycin, a glycosylation inhibitor that leads to the accumulation of
106 unfolded proteins in the ER (Fig. 1C). Finally, we performed ER stress tolerance assays to
107 test the physiological importance of UFMylation in *C. reinhardtii*. *uba5* and *ufl1* mutants were
108 more sensitive to ER stress than the wild type, confirming UFMylation is essential for ER

bioRxiv preprint doi: https://doi.org/10.1101/2022.04.26.489478; this version posted April 26, 2022. The copyright holder for this preprint (which was not certified by peer review) is the author/funder, who has granted bioRxiv a license to display the preprint in perpetuity. It is made available under aCC-BY 4.0 International license.

109 stress tolerance in *C. reinhardtii* (Fig. 1D). Altogether, these findings suggest UFMylation
110 contributes to ER homeostasis across eukaryotes.
111

112 **C53 interacts with UFM1 via the shuffled ATG8 interacting motifs (sAIMs)**

113 In addition to revealing the conservation of the UFMylation pathway in unicellular organisms,
114 our phylogenomic analysis also showed a strong presence-absence correlation between
115 C53 and UFM1 (Fig. 1A). To investigate whether this correlation is due to a functional link
116 between C53 and UFM1, we first performed ConSurf analysis of C53 to estimate the
117 conservation of each residue [25]. C53 has two α-helical domains at the N- and C- termini,
118 connected with an intrinsically disordered region. In contrast to the alpha helical domains,
119 which were highly conserved, the IDR was divergent. However, within the IDR, there were
120 four highly conserved regions that corresponded to the sAIMs (Fig. 2A). To explore a
121 possible connection between UFM1 and the sAIMs, we examined the conservation of
122 individual sAIMs between species with and without UFM1 (Fig. 2B). Although IDR residues
123 are generally not conserved between and within groups, the sAIMs show a strong dichotomy
124 between species with and without UFM1, demonstrating a link between sAIM conservation
125 and the presence of UFM1. In agreement with this, multiple sequence alignment revealed
126 that the C53 IDRs in species lacking UFM1 are consistently shorter relative to UFM1-
127 encoding species, and lack sAIMs (Fig. 2C). To support these findings, we synthesized C53
128 homologs from two species that lack UFM1 (the oomycete *Albugo candida* (Ac) and chytrid
129 *Piromyces finnis* (Pf)) and tested whether they interact with UFM1 or ATG8 using *in vitro*
130 pulldown assays. Both AcC53 and PfC53 were able to interact with Arabidopsis ATG8A and
131 human ATG8 isoform GABARAP (Fig. 2D), but they did not interact with either of the UFM1
132 orthologs tested (Fig. 2E). Their ability to bind ATG8 may be due to the presence of putative
133 cAIMs within the truncated IDRs of both AcC53 and PfC53 (Fig. 2C, D).
134

135 As the phylogenomic analyses suggested that the sAIMs have been retained to mediate
136 C53-UFM1 interaction, we sought to reconstitute the human UFM1-C53 complex using
137 native Mass-Spectrometry (nMS). We found that C53 binds to human UFM1 in a 1:1 or 1:2
138 stoichiometry, similar to the C53-GABARAP interaction (Fig. S4). To map the UFM1
139 interacting region in C53, we performed *in vitro* pulldowns with *Homo sapiens* (Hs) and
140 *Arabidopsis thaliana* (At) C53 truncations. As in the C53-ATG8 interaction, the C53 IDR was
141 necessary for interaction between C53 and UFM1 (Fig. 2F, G). Further individual and
142 combinatorial mutagenesis of the tryptophan residues in sAIMs showed that the UFM1-C53
143 interaction is mediated by sAIMs located in the IDR (Fig. 2H).
144

bioRxiv preprint doi: https://doi.org/10.1101/2022.04.26.489478; this version posted April 26, 2022. The copyright holder for this preprint (which was not certified by peer review) is the author/funder, who has granted bioRxiv a license to display the preprint in perpetuity. It is made available under aCC-BY 4.0 International license.

145 We next asked whether ATG8 and UFM1 bind the sAIMs in a similar manner. First, we
146 performed nMS analysis to test the interaction of HsUFM1 with a canonical AIM (cAIM)
147 peptide [14]. Unlike the UBA5-LIR peptide (GPLHDDNEWNISVVDD), which has been
148 shown to interact with UFM1 [26–28], the cAIM peptide did not appreciably interact with
149 UFM1 (Fig. 3A). Consistently, the cAIM peptide outcompeted the GABARAP-C53 interaction
150 but not the HsUFM1-C53 interaction (Fig. 3B). *C. reinhardtii* proteins behaved similarly;
151 CrC53 interacted with ATG8 in a cAIM-dependent manner and CrUFM1 in a cAIM-
152 independent manner (Fig. S5).
153
154 To further test these interactions, we performed microscopy-based on-bead binding assays.
155 The advantage of this technique is the ability to visualize protein-protein interactions with fast
156 dissociation constants at equilibrium. It can also detect relatively weak, transient interactions
157 [29]. We purified GST-tagged Arabidopsis and human ATG8 and UFM1 proteins and
158 coupled them to the glutathione coated beads (Sepharose 4B, Cytiva). We then tested
159 whether mCherry tagged Arabidopsis and human C53 proteins could bind to the ATG8 or
160 UFM1 coupled beads (Fig. S6A). Arabidopsis and human C53 interacted with wild type
161 ATG8 and UFM1, and HsC53-GABARAP and AtC53-ATG8A interaction was outcompeted
162 with increased concentrations of the cAIM peptide (Fig. 3C and Fig. S6B). In contrast, the
163 cAIM peptide could not outcompete the HsC53-HsUFM1 or AtC53-AtUFM1 interaction (Fig.
164 3D and Fig. S6C). Consistently, the UBA5-LIR peptide and GABARAP were able to disrupt
165 C53-UFM1 interaction (Fig. S6D). Altogether, these results suggested that ATG8 and UFM1
166 bind the sAIMs within C53 IDR, albeit in a different manner.
167

168 Comparative NMR spectroscopy analysis revealed the differences between C53 IDR-169 UFM1 and C53 IDR-ATG8 interaction

170 To elucidate the difference between UFM1 and ATG8 binding to C53 IDR, we performed
171 comparative nuclear magnetic resonance (NMR) spectroscopy analysis. We first obtained
172 backbone resonance assignments of AtC53 IDR. We could assign 89% of the residues in
173 AtC53 IDR. The sAIMs in AtC53 IDR share high sequence homology, therefore we validated
174 the assignments using sAIM1 (AtC53 IDR^{W276A}) and sAIM2 (AtC53 IDR^{W287A}) mutants (Fig.
175 4A, Fig. S7A). The 2D heteronuclear single quantum correlation (HSQC) spectrum of ^{15}N-
176 labelled AtC53 IDR displayed small dispersion of the backbone amide residues, validating its
177 intrinsically disordered nature. The NMR signals are sensitive to their chemical environment;
178 binding of an interaction partner or conformational changes induced by protein-protein
179 interaction shifts the NMR spectra. Moreover, NMR signal intensity drops mainly due to an
180 increase in molecular weight upon complex formation and the chemical exchange that

bioRxiv preprint doi: https://doi.org/10.1101/2022.04.26.489478; this version posted April 26, 2022. The copyright holder for this preprint (which was not certified by peer review) is the author/funder, who has granted bioRxiv a license to display the preprint in perpetuity. It is made available under aCC-BY 4.0 International license.

181 happens at the interaction surface [30–33].

182 Following the backbone assignment, we mapped UFM1 and ATG8 interaction sites in AtC53
183 IDR by acquiring 2D HSQC spectra of ^{15}N-labelled AtC53 IDR in the presence and absence
184 of unlabelled AtUFM1 or ATG8A. Upon AtUFM1 binding, the signals of AtC53 IDR displayed
185 both chemical shift perturbations (CSP) and reduction in their intensity. CSP analysis
186 showed that upon AtUFM1 binding, the signals corresponding to Asp275, Thr279 (sAIM1),
187 Asp286 and Ser297 (sAIM2) and the residues Glu281 and Glu285 that are located between
188 sAIM1 and sAIM2 shifted in a concentration dependent manner (Fig. S7B). Instead, the
189 signals corresponding to Ile274 and Trp276 found in sAIM1, Ile278 and Val280 found in the
190 region between sAIM1 and sAIM2 and Trp287 located in sAIM2 exhibited line broadening
191 and reduced intensity upon binding of AtUFM1 (Fig. 4B). These data confirm that sAIM1 and
192 sAIM2 regions are the major interaction sites for AtUFM1. Notably, the hydrophobic residues
193 between these sAIMs also contributed to the binding. The sAIM1 region showed a significant
194 decrease in signal intensity already at the lowest UFM1 concentration, confirming sAIM1 is
195 the highest affinity binding site for UFM1, followed by sAIM2 region (Fig. 4B-D, S7C). These
196 results are in line with the pulldown assays performed with the Trp to Ala mutants of the
197 sAIMs (Fig. 2H).

198 We next characterized the binding of ATG8A to AtC53 IDR. Upon ATG8A binding, large
199 number of signals in the AtC53 IDR spectrum disappeared or shifted (Fig. 4E-F, Fig. S7D).
200 The signals of the cAIM and its neighbouring residues covering Leu301 to Glu314
201 disappeared or shifted at lowest ATG8A concentration (75 µM), followed by sAIM1 and
202 sAIM2 regions as we titrated increased concentrations of ATG8A (Fig. S7E, Fig. 4E).
203 Importantly, the signals Ile274 and Trp276 in sAIM1, which disappeared upon 75 µM UFM1
204 titration, only disappeared upon 200 µM ATG8A addition, suggesting that while the most
205 preferred binding site for UFM1 is sAIM1, it is cAIM for ATG8A. Similar to UFM1, CSP
206 analysis showed that the signals in sAIM3 region only shifted at highest ATG8A
207 concentration (300 µM) and did not show significant signal intensity reduction, suggesting
208 sAIM3 is a low affinity binding site for both ATG8A and UFM1 (Fig. 4F, G, S7E). Strikingly,
209 residues covering amino acids that precede sAIM1 (265-272) and between cAIM and sAIM3
210 (315-332) experienced at least a 3-fold increase in their signal intensity upon ATG8A titration
211 (Fig. S7E). However, they displayed minor chemical shift perturbations, suggesting these
212 residues do not directly bind ATG8A, but their dynamics change upon ATG8A binding.
213 Altogether, these data suggest that certain regions in AtC53 IDR might be found in a
214 conformational ensemble that is modulated upon binding of ATG8 but not UFM1. Also, in
215 contrast to UFM1 binding, ATG8A binding triggers a conformational change in C53 IDR. In
216 sum, although both UFM1 and ATG8 bind the sAIMs, their binding modes are different.

bioRxiv preprint doi: https://doi.org/10.1101/2022.04.26.489478; this version posted April 26, 2022. The copyright holder for this preprint (which was not certified by peer review) is the author/funder, who has granted bioRxiv a license to display the preprint in perpetuity. It is made available under aCC-BY 4.0 International license.

217 To reveal the binding mode of C53 IDR to UFM1 and ATG8, we next set out to map the
218 binding site of C53 IDR on UFM1 and ATG8 using NMR spectroscopy. The backbone amide
219 residues of HsUFM1 and GABARAP have been assigned previously [34, 35]. We
220 successfully transferred 81% of the available backbone spectral assignments for HsUFM1
221 and 85% for GABARAP to our 2D HSQC spectra, allowing us to characterize the C53
222 interaction with both UFM1 and ATG8. We then acquired 2D HSQC spectra of ^{15}N-labelled
223 UFM1 and ^{15}N-labelled ATG8A/GABARAP in the presence and absence of unlabelled C53
224 IDR. The CSP analysis showed that the signals of Met1, Ser5, Ile8, Lys19, Glu25, Ala31,
225 Lys34, Phe35, Ala36 and Thr67 of HsUFM1 shifted upon HsC53 IDR binding (Fig. S8A-C).
226 Additional residues such as Val32, Glu39, Thr62, Ala63, Gly64 and Asn65 also experienced
227 lower, yet important CSPs indicating a minor contribution of these residues for C53 IDR
228 interaction (Fig. S8C). When we mapped CSPs onto the three-dimensional structure of
229 HsUFM1, we observed a well-defined interaction site on the UFM1 surface covering the α-
230 helix 1 (31-36) and α-helix 2 (62-67), with contributions from residues in β-strand 1 (Ser5,
231 Ile8) and β-strand 2 (Lys19) (Fig. S8D). The AtC53 IDR binding site converges to a region
232 that is involved in the interaction with the UBA5 LIR/UFIM [26], suggesting C53 sAIM
233 interacts with UFM1 in a similar manner to UBA5 LIR/UFIM. To test whether C53 IDR and
234 UBA5 bind UFM1 similarly in plants, we acquired 2D HSQC spectra of ^{15}N-labelled AtUFM1
235 in the presence and absence of unlabelled AtC53 IDR or AtUBA5 LIR/UFIM peptide. Most of
236 the signals that shifted upon AtC53 IDR binding, followed the same trend when AtUFM1 is
237 titrated with AtUBA5 LIR/UFIM, consistent with a conserved binding mode (Fig. S8E).
238 Furthermore, mutation of the tryptophan residue in sAIM1 (AtC53 IDR^{W276A}) reduced
239 chemical shift perturbations in AtUFM1 spectrum, supporting its dominant role in AtUFM1
240 binding (Fig. 4C, D, S8E).

241 We next analysed the HsC53 IDR-GABARAP interaction. The CSP analysis indicated
242 GABARAP residues Tyr25, Val33, Glu34, Lys35, Ile41, Asp45, Lys46, Tyr49, Leu50 and
243 Phe60 formed intermolecular contacts with C53 IDR (Fig. S9A-C). Additional residues such
244 as Lys20, Ile21, Lys23, Ile32, Asp54, Phe62 and Ile64 displayed smaller CSPs indicating a
245 minor contribution of these residues in the interaction (Fig. S9C). Mapping of CSPs onto the
246 three-dimensional structure of GABARAP highlighted the well-defined LIR docking site (LDS)
247 on the GABARAP surface (Fig. S9D), composed of α-helix 2 (20-25), β-strand 2 (49-52) and
248 α-helix 3 (56-68) residues. Canonical LIR/AIM binding involves the formation of an
249 intermolecular β-sheet with β-strand 2 on ATG8-family proteins and the accommodation of
250 the aromatic and aliphatic residues on two hydrophobic pockets (HP): HP1, which comprises
251 residues in α-helix 2 and β-strand 2, and HP2, formed between the β-strand 2 and α-helix 3,
252 commonly referred to as W and L-site, respectively [36]. However, C53 IDR binding to

bioRxiv preprint doi: https://doi.org/10.1101/2022.04.26.489478; this version posted April 26, 2022. The copyright holder for this preprint (which was not certified by peer review) is the author/funder, who has granted bioRxiv a license to display the preprint in perpetuity. It is made available under aCC-BY 4.0 International license.

253 GABARAP also induces CSPs for residues in β-strand 1 (28-35), closed to α-helix 1 (Fig.
254 S9D). This region has been reported to undergo conformational changes that leads to the
255 formation of a new hydrophobic pocket (HP0) in GABARAP surface upon HsUBA5 LIR/UFIM
256 binding [27]. This suggests, like UFM1, C53 sAIM-ATG8 binding mechanism is similar to
257 UBA5 LIR/UFIM. We confirmed that these binding features are also conserved in plants by
258 acquiring the 2D HSQC spectra of ^{15}N-labelled ATG8A in the presence and absence of
259 unlabelled AtC53 IDR or AtUBA5 LIR/UFIM peptide. As for UFM1, most of the signals that
260 shifted followed the same trend upon titration with either C53 IDR or UBA5 LIR/UFIM,
261 demonstrating both motifs bind to a similar site on ATG8 (Fig. S9E). However, unlike UFM1,
262 mutating the aromatic residue in sAIM1 (AtC53 IDR^{W276A}) did not reduce CSPs in ATG8A
263 spectrum (Fig. S9D), since binding can proceed via sAIM2 and cAIM residues.

264

265 **C53 sAIMs are crucial for C53-mediated autophagy and ER stress tolerance.**

266 Our evolutionary and structural analyses suggest that the sAIMs evolved and were selected
267 for their ability to interact with both UFM1 and ATG8. What would happen if we converted
268 sAIMs to cAIMs? We hypothesized that converting sAIMs into cAIMs would reduce the
269 affinity of C53 towards UFM1 and lead to C53 autoactivation, even in the absence of ER
270 stress (Fig. 5A). To test this hypothesis, we generated an AtC53^{cAIM} mutant by re-ordering
271 the residues of each sAIM from IDWD to WDDI. We first assessed the interaction of
272 AtC53^{cAIM} with ATG8A by *in vitro* pulldowns. AtC53^{cAIM} bound ATG8A stronger than the wild
273 type C53 protein. Like the wild type C53 protein, AtC53^{cAIM} interacted via the LIR Docking
274 Site (LDS), as observed by competition with cAIM peptide and loss of interaction in the
275 ATG8^{LDS} mutant (Fig. 5B). On the other hand, AtC53^{cAIM} almost completely lost its ability to
276 bind UFM1, consistent with the dependence of UFM1-binding on the sAIMs (Fig. 5C).

277

278 To further corroborate our *in vitro* pulldown assays, we performed quantitative on-bead
279 binding assays. GST-ATG8 and GST-GABARAP recruited C53^{cAIM} mutant 22% (mean) and
280 35% (mean) more efficiently than the respective C53 wild type proteins (Fig. 5D, 5E, S10A,
281 S10B). C53^{sAIM} mutant (with inactivated sAIMs) was instead recruited 74% (mean) and 78%
282 (mean) less to GST-ATG8 and GST-GABARAP, respectively (Fig. 5D, 5E, S10A, S10B). In
283 addition to ATG8, C53 also interacts with the scaffold protein FIP200/ATG11 [37, 38]. We
284 therefore tested the binding affinities of C53 and C53^{cAIM} to FIP200. Similar to our
285 observations with ATG8, HsC53^{cAIM} displayed a stronger interaction with FIP200 than wild
286 type HsC53. Similar to ATG8, FIP200 interaction was also lost in C53^{sAIM} mutant (Fig. S11).
287 These results demonstrate that converting sAIM to cAIM increases the affinity of C53
288 towards ATG8 and decreases its affinity to UFM1.

bioRxiv preprint doi: https://doi.org/10.1101/2022.04.26.489478; this version posted April 26, 2022. The copyright holder for this preprint (which was not certified by peer review) is the author/funder, who has granted bioRxiv a license to display the preprint in perpetuity. It is made available under aCC-BY 4.0 International license.

289
290 We next explored the physiological consequences of sAIM to cAIM conversion. We
291 complemented an *Arabidopsis thaliana c53* mutants with either C53-GFP, C53^{sAIM}-GFP, or
292 C53^{cAIM}-GFP fusions. Consistent with our *in vitro* data, *in vivo* pull-down assays showed that
293 C53^{cAIM}-GFP had a stronger interaction with ATG8 than C53-GFP. On the contrary, the
294 association between C53^{cAIM}-GFP and UFM1 was weaker than between C53-GFP and
295 UFM1 (Fig. 5F, S12A, S12B).
296
297 Under normal conditions, Arabidopsis C53 predominantly has a diffuse cytoplasmic
298 localization pattern. Upon ER stress, it is recruited to the ATG8-labelled autophagosomes
299 [14]. Consistent with our *in vivo* pull-down results, C53^{cAIM}-mCherry formed puncta even
300 under normal conditions, suggesting it associates with ATG8 and recruited to the
301 autophagosomes even in the absence of stress. Altogether, these findings suggest sAIM to
302 cAIM conversion leads to the premature activation of C53-mediated autophagy (Fig. 5G).
303
304 Finally, using tunicamycin plate assays, we measured ER stress tolerance of C53^{cAIM}
305 expressing Arabidopsis plants. Tunicamycin is a glycosylation inhibitor that is commonly
306 used to induce ER stress in plants, which leads to the shortening of the roots in *Arabidopsis*
307 *thaliana* [39]. Compared to wild type complemented plants, C53^{cAIM} expressing Arabidopsis
308 lines formed shorter roots even under control conditions (Fig. 5H). This suggests, premature
309 activation of C53 is detrimental for plant growth, likely due to the degradation of C53 without
310 the bound cargo. The root length was further reduced in tunicamycin containing plates,
311 indicating the inability to degrade C53 cargo that arise upon ER stress is detrimental for
312 plants. Taken together, our results illustrate that C53's ability to bind UFM1 and ATG8, which
313 is encoded in sAIM regions, is crucial for its function and ER stress tolerance.
314

315 Discussion

316 Despite the discovery of UFMylation almost two decades ago, its structural basis, the full
317 spectrum of UFMylated substrates, and its physiological role are still not fully resolved [17,
318 40]. Studies in metazoans and our recent work have shown that UFMylation is involved in a
319 wide range of homeostatic pathways, including ER stress tolerance, immunity, autophagy,
320 lipid droplet biogenesis, and the DNA damage responses [14, 15, 23, 41–46]. In ER
321 homeostasis, UFMylation is activated by stalling of ER-bound ribosomes and brings about
322 the degradation of incomplete polypeptides, which can be toxic for the cell [14, 23]. Limited
323 phylogenetic analysis, comparing yeast to plants and metazoans, suggested that the
324 pathway had evolved in multicellular eukaryotes and could have facilitated the protein
325 synthesis burden that arises during biogenesis of the extracellular matrix [22]. However, our

bioRxiv preprint doi: https://doi.org/10.1101/2022.04.26.489478; this version posted April 26, 2022. The copyright holder for this preprint (which was not certified by peer review) is the author/funder, who has granted bioRxiv a license to display the preprint in perpetuity. It is made available under aCC-BY 4.0 International license.

326 extensive phylogenomic analysis, in agreement with a recent study, clearly shows that
327 UFMylation did not evolve in multicellular eukaryotes, but was secondarily lost in fungi and
328 other lineages [47] (Fig. 1). Indeed, many single-celled organisms including *Chlamydomonas*
329 harbour a full complement of UFMylation components in their genome, whereas certain
330 multicellular lineages, such as kelp (Phaeophyceae), have lost the majority of the pathway.
331 We provide biochemical and physiological evidence showing UFMylation is functional in
332 *Chlamydomonas*, unequivocally refuting the idea that UFMylation evolved only in
333 multicellular organisms (Fig. 1). Our evolutionary analysis also highlights why we should
334 move beyond yeast and metazoans and instead consider the whole tree of life when using
335 evolutionary arguments to guide biological research. Our phylogenetic analysis also
336 revealed that in addition to the Fungi, several algal groups, and pathogens such as
337 *Plasmodium*, *Entamoeba,* and *Trichomonas* have also lost UFMylation. So, how do
338 pathogens and parasitic fungi resolve stalled ER-bound ribosomes? Comparative studies
339 addressing these questions could provide potential translational avenues for developing
340 genetic or chemical means to prevent infections.
341
342 Another conclusion of our phylogenetic studies is the tight connection between the presence
343 of sAIMs located in the C53 IDR and UFM1. Species that lack UFM1 also lost the sAIMs in
344 C53 (Fig. 2). Using biochemical and structural approaches, we found that sAIMs form
345 versatile docking sites that can interact with both UFM1 and ATG8. UFM1 interaction is
346 mostly mediated by sAIM1 and sAIM2, whereas ATG8 interaction is driven by the cAIM,
347 sAIM1 and sAIM2 (Fig. 2, Fig. 4). It is surprising that the sAIM3, which is highly similar to
348 sAIM1/2 does not show significant binding to UFM1. A plausible explanation is that the
349 aspartic acid at the second position in sAIM1/2 (I**D**WD) motif play an important role for the
350 interaction, and having a serine instead of an aspartic acid in sAIM3 (I**S**WD) weakens the
351 binding. Consistently, the NMR analyses showed that the signals of the residues neighboring
352 sAIMs showed significant chemical shifts suggesting that they also contribute to the
353 interaction with both UFM1 and ATG8.

354
355 The NMR experiments also revealed that UFM1 and ATG8 binding induce distinct
356 conformational changes on C53 IDR (Fig. S7). UFM1 binding reduces the overall signal
357 intensity with further reduction at the direct binding sites corresponding to sAIM1 and sAIM2.
358 On the contrary, ATG8 binding leads to a local signal intensity drop at the sAIM1-2 and cAIM
359 but increases the signal intensity of residues that do not interact with ATG8. These data
360 suggest that upon ATG8 binding C53 IDR becomes more dynamic, potentially allowing it to
361 bind the autophagic cargo. This structural rearrangement could also affect the E3 ligase

bioRxiv preprint doi: https://doi.org/10.1101/2022.04.26.489478; this version posted April 26, 2022. The copyright holder for this preprint (which was not certified by peer review) is the author/funder, who has granted bioRxiv a license to display the preprint in perpetuity. It is made available under aCC-BY 4.0 International license.

362 activity of the UFL1 enzyme complex. Indeed, a recent study has shown that C53 negatively
363 regulates UFMylation activity, when bound to the UFL1-DDRGK1 complex [21]. Altogether,
364 these results indicate that evolution of suboptimal ATG8 interacting motifs enabled C53 to
365 interact with another regulatory protein, UFM1, creating an autoinhibition mechanism that
366 regulates ER-phagy. This illustrates how complex regulatory circuits could evolve by
367 shuffling existing short linear motifs.

368 Interestingly, another non-canonical motif on UBA5, the E1 enzyme of the UFMylation
369 cascade, can also bind both UFM1 and ATG8 through similar binding pockets (Fig. S8, Fig.
370 S9). Removing or mutating UBA5 LIR affects the kinetics of UFMylation and the GABARAP
371 dependent recruitment of UBA5 to ER upon stress [27]. Our findings go a step further and
372 show that non-canonical motifs on C53 are essential for organismal fitness, as converting
373 sAIMs to canonical AIMs leads to reduced ER stress tolerance in *Arabidopsis thaliana* (Fig.
374 5H). Further *in vitro* reconstitution studies that involve the UFMylation machinery, C53
375 receptor complex, and stalled membrane-bound ribosomes are necessary to understand the
376 dynamic changes that lead to C53 activation, which would explain how UFMylation and
377 autophagy intersect at the ER.
378
379 In summary, our data converge on the model that UFM1 and ATG8 compete for C53 binding
380 via the shuffled ATG8 interacting motifs [14]. Under normal conditions, C53 is bound to
381 UFM1, keeping it inactive. Upon stress, UFM1 is displaced by ATG8, leading to structural
382 rearrangements that trigger C53-mediated autophagy. These results provide a mechanism
383 where the cell keeps selective autophagy pathways inactive under normal conditions to
384 prevent the spurious degradation of healthy cellular components and saves the energy that
385 is required to form autophagosomes.
386

387 ## Acknowledgements

388 We thank Vienna Biocenter Core Facilities (VBCF) Protein Chemistry, Biooptics, Plant
389 Sciences, Molecular Biology, and Protein Technologies. We acknowledge funding from
390 Austrian Academy of Sciences, Austrian Science Fund (FWF, P 32355, P 34944), Austrian
391 Science Fund (FWF- SFB F79), Vienna Science and Technology Fund (WWTF, LS17-047),
392 Marie Curie Fellowship to NZ. RB acknowledges support of a UKRI Future Leaders
393 Fellowship (Grant Reference MR/T020970/1) and a Chancellor's Fellowship from the
394 University of Strathclyde. The IMP is supported by Boehringer Ingelheim. We thank J.
395 Matthew Watson and members of the Dagdas lab for the critical reading and editing of the
396 manuscript. We are thankful to Max Perutz Labs NMR facility and Georg Kontaxis for the
397 NMR measurements. We thank Mathias Madalinski, Zsuzsanna Muhari-Portik for peptide

bioRxiv preprint doi: https://doi.org/10.1101/2022.04.26.489478; this version posted April 26, 2022. The copyright holder for this preprint (which was not certified by peer review) is the author/funder, who has granted bioRxiv a license to display the preprint in perpetuity. It is made available under aCC-BY 4.0 International license.

398 synthesis. We also thank Orla Dunne, Arthur Sedivy, David Drechsel for help in protein
399 purification and characterization experiments.

400

401 **Contributions.** LP, VM, NZ, EK and YD conceived and designed the project. NI performed
402 the phylogenomic analysis. LP and SR performed the *Chlamydomonas reinhardtii* related
403 experiments. LP, VM and JSM performed *in vitro* biochemical and biophysical assays. RB
404 performed native mass spectrometry experiments. TL trained the deep learning model for
405 agarose bead recognition. VM and HH performed the NMR spectroscopy experiments. NZ,
406 MS and NG performed *Arabidopsis thaliana* related experiments. SM, TR, TC, SR, EK and
407 YD supervised the project. LP, VM, NZ, NI, EK and YD wrote the manuscript with input from
408 all the authors.

409

410 **Competing interest declaration.** The authors declare no competing financial interests.

411

bioRxiv preprint doi: https://doi.org/10.1101/2022.04.26.489478; this version posted April 26, 2022. The copyright holder for this preprint (which was not certified by peer review) is the author/funder, who has granted bioRxiv a license to display the preprint in perpetuity. It is made available under aCC-BY 4.0 International license.

412 ## Materials and Methods

413 ### Phylogenomic analysis

414 To reconstruct the evolutionary history of the UFMylation pathway, we searched for
415 UFMylation proteins (including RPL26) in 151 eukaryotic datasets comprising 149 genomes
416 and two transcriptomes from the dinoflagellates *Togula jolla* and *Polarella glacialis*
417 (Supplementary Data S1). Initially, *Homo sapiens* proteins were used as queries to search
418 predicted proteomes using Diamond BLASTp v2.0.9 (E-value < 10^{-5}, ultra-sensitive mode)
419 [48]. Multiple sequence alignments were then inferred using MAFFT v7.490 (-auto) and
420 trimmed using trimAl v1.4 with a gap-threshold of 30%, before preliminary phylogenies were
421 generated using IQ-Tree v2.1.2 (LG4X model, fast mode) [49–51]. The resulting phylogenies
422 were annotated using SWISS-PROT (version 2022_01) and Pfam (version 35.0) and then
423 interpreted in FigTree v1.4.2. From the phylogeny, orthologs were identified, extracted, and
424 used as queries for a second iteration of BLAST searching as described above [52–54]. To
425 improve search sensitivity, the orthologs identified using BLAST were then used to generate
426 profile hidden Markov models (HMMs). Initially, the proteins were re-aligned with the
427 structurally informed aligner MAFFT-DASH with the L-INS-i algorithm and were then trimmed
428 with a gap-threshold of 10% [55]. HMMs were then generated from the alignments and used
429 to re-search the proteomic datasets using HMMER v3.1b2 (E-value < 10^{-5}) [56]. The
430 identified homologs were once again aligned, trimmed, and assessed phylogenetically,
431 facilitating the removal of paralogs. Lastly, to account for the possibility that proteins could
432 be missing due to genomic mis-annotation, proteins identified from the predicted proteomes
433 were used as queries for tBLASTn (E-value < 10^{-5}) searches against eukaryotic genomes
434 and protein predictions were generated using Exonerate v2.2 (see
435 https://github.com/nickatirwin/Phylogenomic-analysis) [57]. Newly predicted proteins were
436 combined with the previously identified proteins and were once again phylogenetically
437 screened for paralogs. The presence and absence of the resulting orthologs was plotted
438 across a eukaryotic phylogeny using ITOL v6 with taxonomic information inferred from NCBI
439 Taxonomy following adjustments made based on recent phylogenomic analyses [58–60].

440 To investigate the sequence conservation of C53 and RPL26, multiple sequence alignments
441 were generated from the identified orthologs using MAFFT with the L-INS-i algorithm. The
442 alignments were then trimmed using a gap-threshold of 30% and fragmented sequences
443 with less than 50% data were filtered out. In the case of C53, alignment of the poorly
444 conserved intrinsically disordered region (IDR) was improved through re-alignment using
445 MUSCLE v3.8 implemented in AliView v1.26 [61, 62]. For C53, phylogenetic analyses were
446 conducted using IQ-Tree and substitution models were selected using ModelFinder

bioRxiv preprint doi: https://doi.org/10.1101/2022.04.26.489478; this version posted April 26, 2022. The copyright holder for this preprint (which was not certified by peer review) is the author/funder, who has granted bioRxiv a license to display the preprint in perpetuity. It is made available under aCC-BY 4.0 International license.

447 (LG+F+R6) [63]. The phylogeny and C53 alignment were then used in an analysis using
448 ConSurf to examine sequence conservation. Likewise, both the C53 and RPL26 alignments
449 were used to assess sequence conservation and divergence between species with and
450 without UFM1 using TwinCons (using the LG substitution model and Voronoi clustering) [64].
451 Lastly, alignment logos for the C53 shuffled AIMs were generated with Skylign using
452 weighted counts [65].

453 **Cloning procedures**

454 Constructs for *Arabidopsis thaliana* and *Escherichia coli* transformation were generated
455 using the GreenGate (GG) cloning method [66]. Plasmids used are listed in materials
456 section. The coding sequence of genes of interest were either ordered from Twist
457 Biosciences or Genewiz or amplified from Col-0 using the primers listed in the materials
458 section. The internal *Bsa*I sites were mutated by site-directed-mutagenesis without affecting
459 the amino acid sequence.

460 ***Chlamydomonas reinhardtii* genomic DNA extraction**

461 The following protocol was adapted from *Perlaza K., et al. 2019* [67]. A 6 ml aliquot of a
462 liquid TAP culture in mid-log phase was spun down, and the media was decanted. The pellet
463 was resuspended in 400 µl of water and then 1 volume of DNA lysis buffer was added (200
464 mM Tris HCl pH 8.0, 6% SDS, 2 mM (EDTA)). To digest proteins, 5 µ of 20 mg/ml
465 proteinase K (Thermo Fischer) was added and allowed to incubate at Room Temperature
466 (RT) for 15 min. 200 µl of 5M NaCl was then added and mixed gently. Next, to selectively
467 precipitate nucleic acids, 160 µl of 10% CTAB in 0.7 M NaCl was added and allowed to sit
468 for 10 min at 65°C with gentle agitation. Two or more consecutive rounds of DNA extraction
469 using ultrapure phenol:chloroform:isoamyl alcohol (25:24:1, v/v/v) were performed to achieve
470 a clean interphase. Then, the upper aqueous phase was retained and mixed with 1 volume
471 of 2-propanol. This was mixed gently for 15 min at RT. Then it was spun down for 30 min at
472 21,000 x g at 4°C. The supernatant was removed and 1 volume of ice-cold 70% ethanol was
473 added and mixed with the pellet. This mixture was spun down for 15 min at 21,000 x g. The
474 supernatant was removed, and the DNA precipitate was dried in a speed-vac for about 10–
475 25 min and resuspended in 40 µl of nuclease-free water.

476 The purity of the genomic DNA preparation was assessed using a spectrophotometer,
477 ensuring absorbance ratios at 260/280 nm and 260/230 nm to be ~1.8 and ~2.0,
478 respectively, prior to using the genomic DNA preparation for most of the follow-up
479 applications.

480 **Genotyping of the *Chlamydomonas reinhardtii* mutants**

bioRxiv preprint doi: https://doi.org/10.1101/2022.04.26.489478; this version posted April 26, 2022. The copyright holder for this preprint (which was not certified by peer review) is the author/funder, who has granted bioRxiv a license to display the preprint in perpetuity. It is made available under aCC-BY 4.0 International license.

481 The insertion of the mutagenic cassette (PARO) in the UBA5 and UFL1 loci was verified by
482 PCR by using primers designed to anneal inside and outside of the PARO cassette, using
483 KOD Extreme Hot Start DNA Polymerase (Sigma). The PCR products were run on 1 % (w/v)
484 agarose. The primer sequences and expected PCR products can be found in *Materials*.

485 ***Chlamydomonas reinhardtii* in vivo UFMylation assays**

486 Cell cultures were grown in liquid TAP medium in 100 ml Erlenmeyer flasks for about two
487 days to an OD_{600} of 1.5-2. These cultures were then transferred to fresh liquid TAP medium,
488 with or without 0.2 mg/l Tunicamycin, to a final OD_{600} of 0.1. After either 12 hours or 24 hours
489 of treatment, 5 ml of cell culture was spun down, flash frozen in liquid nitrogen and stored at
490 -70 °C.

491 The pellets were thawed and resuspended in 150 µl of SDS-lysis buffer (100 mM Tris-HCl
492 pH 8.0, 600 mM NaCl, 4% SDS, 20 mM EDTA, freshly supplied with Roche Protease
493 Inhibitors). Samples were vortexed for 10 min at RT and centrifuged at maximum speed for
494 15 min at 4°C to remove the cell debris. The supernatant, containing a total extract of
495 denatured proteins was transferred to a new eppendorf tube, a 5 µl aliquot was saved for
496 BCA quantification and diluted accordingly.

497 5X SDS-loading buffer (250 mM Tris-HCl pH 6.8, 5% SDS, 0.025% bromophenol blue, 25%
498 glycerol), freshly supplied with 5% of β-mercaptoethanol, was added to the extract and
499 denatured at 90°C for 10 min. The samples were loaded on 4–20% SDS-PAGE gradient gel
500 (BioRad) and electrophoresis was run at 100V for 1.5 hr.

501 ***Chlamydomonas reinhardtii* survival assays**

502 Cell cultures were grown in liquid TAP medium in a 100 ml Erlenmeyer flask for about two
503 days to an OD_{600} of 1.5-2. These cultures were then transferred to fresh liquid TAP medium,
504 with or without 0.2 mg/l Tunicamycin, to a final OD_{600} of 0.1. After 24, 48 and 72 hours of
505 treatment, the optical density (OD) of the cultures was measured using a spectrophotometer
506 at 600 nm.

507 ***Arabidopsis thaliana* plant materials and growth conditions**

508 The Columbia-0 (Col-0) accession of *Arabidopsis* was used in this study unless otherwise
509 indicated. *Arabidopsis* mutants used in this study are listed in the materials section.
510 Generation of transgenic *Arabidopsis* plants was carried out by *Agrobacterium*-mediated
511 transformation [68].

512 Seeds were imbibed at 4°C for 3 days in dark. For the co-immunoprecipitation experiment,
513 seeds were sterilized and cultured in liquid 1/2 MS medium containing 1% sucrose with

bioRxiv preprint doi: https://doi.org/10.1101/2022.04.26.489478; this version posted April 26, 2022. The copyright holder for this preprint (which was not certified by peer review) is the author/funder, who has granted bioRxiv a license to display the preprint in perpetuity. It is made available under aCC-BY 4.0 International license.

514 constant shaking under continuous LED light. For the root length measurements, seeds are
515 sterilized and sown on sucrose-free 1/2 MS agar plates and grown at 22°C at 60% humidity
516 under continuous white light at 12/12-hour light/dark cycle.

517 **Root length quantification**

518 Seedlings were grown vertically for 7 days on sucrose-free 1/2 MS plates supplemented with
519 indicated chemicals. Plates were photographed using a Canon EOS 80D camera. The root
520 length was measured using ImageJ software (version: 2.1.0/1.53c) for further analysis [69].

521 ***In vivo* co-immunoprecipitation**

522 *Arabidopsis* seedlings were cultured in liquid 1/2 MS medium with 1% sucrose for 7-8 days.
523 These seedlings were then treated for additional 16 hours in 1/2 MS liquid medium with 1%
524 sucrose supplemented with DMSO or tunicamycin, respectively. About 1-2 mg plant material
525 was harvested and homogenized using liquid nitrogen and immediately dissolved in grinding
526 buffer (50 mM Tris-HCl, pH 7.5, 150 mM NaCl, 10 mM $MgCl_2$, 10% glycerol, 0.1% Nonidet
527 P-40, Protease Inhibitor Cocktail tablet) by vortex. Plant lysates were cleared by
528 centrifugation at 16,000g for 5 min at 4°C several times. After binding to Protein A Agarose,
529 3 mg total plant protein were incubated with 25 μL GFP-Trap Magnetic Agarose beads
530 (ChromoTek) at 4°C for 2.5 hours. Pellets were washed with grinding buffer for six times,
531 boiled for 10 min at 95°C prior to immunoblotting with the respective antibodies.

532 **Confocal microscopy**

533 *Arabidopsis* roots were imaged using a Zeiss LSM780 confocal microscope with an
534 Apochromat 20x objective lens at 2 X magnification. Z-stack merged images with 2 μm
535 thickness per Z-stack were used for analysis. At least 5 Z-stacks were used for puncta
536 quantification and image presentation. Confocal images were processed with ImageJ
537 software [69].

538 **Quantification of confocal micrographs**

539 ImageJ software (version: 2.1.0/1.53c) [69] is used for autophagic puncta number
540 quantification. ATG8A puncta colocalized C53 punctuates were manually mounted for each
541 stack and added for all stacks for a single image. Autophagosome number per normalized Z-
542 stack was calculated by total autophagosome number of a certain image divided by the
543 relative root area.

544 **Western blotting**

545 Blotting on nitrocellulose membranes was performed using a semi-dry Turbo transfer blot

bioRxiv preprint doi: https://doi.org/10.1101/2022.04.26.489478; this version posted April 26, 2022. The copyright holder for this preprint (which was not certified by peer review) is the author/funder, who has granted bioRxiv a license to display the preprint in perpetuity. It is made available under aCC-BY 4.0 International license.

546 system (BioRad). Membranes were blocked with 5% skimmed milk or BSA in TBS and 0.1%
547 Tween 20 (TBS-T) for 1 hour at room temperature or at 4°C overnight. This was followed by
548 incubation with primary and subsequent secondary antibody conjugated to horseradish
549 peroxidase. After five 5 min washes with TBS-T, the immune-reaction was developed using
550 either Pierce™ ECL Western Blotting Substrate (ThermoFisher) or SuperSignal™ West Pico
551 PLUS Chemiluminescent Substrate (ThermoFisher) and detected with either ChemiDoc
552 Touch Imaging System (BioRad) or iBright Imaging System (Invitrogen).

553 **Western blot image quantification**

554 Protein bands intensities were quantified with ImageJ [69]. Equal rectangles were drawn
555 around the total protein gel lane and the band of interest. The area of the peak in the profile
556 was taken as a measure of the band intensity. The protein band of interest was normalized
557 for the total protein level of the protein lane used as a bait. Average relative intensities and a
558 standard error of three independent experiments were calculated.

559 **Protein expression and purification for biochemical assays**

560 Recombinant proteins were produced using *E. coli* strain Rosetta2 (DE3) pLysS grown in 2x
561 TY media at 37°C to an A_{600} of 0.4–0.6 followed by induction with 300 μM IPTG and
562 overnight incubation at 18°C.

563 For *in vitro* UFMylation assays, *in vitro* pulldowns, and *in vitro* protein-protein microscopy
564 binding assays pelleted cells were resuspended in lysis buffer (100 mM HEPES pH 7.5, 300
565 mM NaCl) containing protease inhibitors (Complete™, Roche) and sonicated. The clarified
566 lysate was first purified by affinity, by using HisTrap FF (GE HealthCare) columns. The
567 proteins were eluted with lysis buffer containing 500 mM imidazole. The eluted fraction was
568 buffer exchanged to 10 mM HEPES pH 7.5, 100 mM NaCl and loaded either on Cation
569 Exchange, Resource S, or Anion Exchange, Resource Q, chromatography columns. The
570 proteins were eluted from 5 to 55 % of Ion exchange buffer B (10 mM HEPES pH 7.5, 1 M
571 NaCl by NaCl) gradient in 20 CV. Finally, the proteins were separated by Size Exclusion
572 Chromatography with HiLoad® 16/600 Superdex® 200 pg or HiLoad® 16/600 Superdex®
573 75 pg, which were previously equilibrated in 50 mM HEPES pH 7.5, 150 mM NaCl.

574 The proteins were concentrated using Vivaspin concentrators (3000, 5000, 10000 or 30000
575 MWCO). Protein concentration was calculated from the UV absorption at 280 nm by DS-11
576 FX+ Spectrophotometer (DeNovix).

577 **Protein expression and purification for Nuclear Magnetic Resonance (NMR)**
578 **spectroscopy**

bioRxiv preprint doi: https://doi.org/10.1101/2022.04.26.489478; this version posted April 26, 2022. The copyright holder for this preprint (which was not certified by peer review) is the author/funder, who has granted bioRxiv a license to display the preprint in perpetuity. It is made available under aCC-BY 4.0 International license.

579 All recombinant proteins were produced using *E. coli* strain Rosetta2 (DE3) pLysS.
580 Transformed cells were grown in 2x TY media supplemented with 100 µg/mL spectinomycin
581 at 37ºC to log phase (OD_{600} 0.6-0.8), followed by induction with 300 µM isopropyl β-D-1-
582 thiogalactopyranoside (IPTG) and incubation at 18ºC overnight. Recombinant isotopically
583 labelled proteins used for Nuclear Magnetic Resonance (NMR) spectroscopy were grown in
584 M9 minimal media as previously described [70] supplemented in the presence of 100 µg/mL
585 spectinomycin at 37ºC to log phase (OD_{600} 0.6-0.8), followed by induction with 600 µM
586 isopropyl β-D-1-thiogalactopyranoside (IPTG) and incubation at 18ºC overnight. Cells were
587 harvested by centrifugation and resuspended in lysis buffer of 100 mM Sodium Phosphate
588 (pH 7.0), 300 mM NaCl, 20 mM imidazole supplemented with Complete-EDTA-Free
589 Protease Inhibitor (Roche) and benzonase. Cells were lysed by sonication and lysate was
590 clarified by centrifugation at 20,000 x g. The clarified lysate was loaded on a HisTrapFF (GE
591 Healthcare) column pre-equilibrated with the lysis buffer. Proteins were washed with lysis
592 buffer for 10 CV and eluted with lysis buffer containing 500 mM Imidazole. The eluted
593 fraction was buffer exchanged to 10mM Sodium Phosphate (pH 7.0), 50 mM NaCl and
594 loaded either on Cation Exchange (ResourceS, Cytiva) or Anion Exchange (ResourceQ,
595 Cytiva) chromatography columns. The proteins were eluted by NaCl gradient (50% in 20
596 CV). Samples were further purified by size-exclusion chromatography with HiLoad 16/600
597 Superdex 200 pg or HiLoad 16/600 Superdex 75 pg (GE Healthcare) with 50 mM Sodium
598 Phosphate (pH 7.0), 100 mM NaCl. The proteins were concentrated using VivaSpin
599 concentrators (3000, 5000, 10000, or 30000 MWCO). Protein concentration was calculated
600 from the UV absorption at 280 nm by DS-11 FX+ Spectrophotometer (DeNovix) or at 205nm
601 by Jasco V-750 UV-Visible Spectrophotometer.

602 ***In vitro* UFMylation assays**

603 CrUBA5, CrUFC1 and UFM1 were mixed to a final concentration of 5 µM, 5 µM and 20 µM
604 respectively in a buffer containing 25 mM HEPES pH 7.5, 150 mM NaCl and 10 mM $MgCl_2$.
605 The enzymatic reaction was started by adding ATP to a final concentration of 5 µM. The
606 enzymatic mixture was incubated for 1 hour at 37°C and then stopped with the addition of
607 non-reducing Laemmli Loading Buffer. Beta-MercaptoEthanol (BME) was added only where
608 specified to reduce UBA5-UFM1 or UFC1-UFM1 thioester bond. The samples were loaded
609 on 4–20% SDS-PAGE gradient gel (BioRad) and electrophoresis was run at 100V for 1.5 hr.

610 ***In vitro* pulldowns**

611 For pulldown experiments, 5 µl of glutathione magnetic agarose beads (Pierce Glutathione
612 Magnetic Agarose Beads, Thermo Scientific) were equilibrated by washing them two times
613 with wash buffer (100 mM Sodium Phosphate pH 7.2, 300 mM NaCl, 1 mM DTT, 0.01% (v/v)

bioRxiv preprint doi: https://doi.org/10.1101/2022.04.26.489478; this version posted April 26, 2022. The copyright holder for this preprint (which was not certified by peer review) is the author/funder, who has granted bioRxiv a license to display the preprint in perpetuity. It is made available under aCC-BY 4.0 International license.

614 IGEPAL). Normalized *E. coli* clarified lysates or purified proteins were mixed, according to
615 the experiment, added to the washed beads and incubated on an end-over-end rotator for 1
616 hour at 4°C. Beads were washed five times with 1 ml wash buffer. Bound proteins were
617 eluted by adding 50 µl Laemmli buffer. Samples were analyzed by western blotting or
618 Coomassie staining.

619 **Microscopy-based on-bead protein-protein interaction assays**

620 Glutathione Sepharose 4B bead slurry (Cytiva, average diameter 90 µm) was washed and
621 diluted 10 times in HEPES buffer (25 mM HEPES pH 7.5, 150 mM NaCl, 1 mM DTT). The
622 beads were then incubated for 30 min at 4°C (16 rpm horizontal rotation) with GST-tagged
623 bait proteins (2 µM of GST, GST-FIP200 CD, GST-ATG8A, GST-GABARAP, GST-AtUFM1,
624 GST-HsUFM1). The beads were washed 5 times in 10 times the bead volume of HEPES
625 buffer. The buffer was removed, and the beads were resuspended 1:20 in HEPES buffer. 10
626 µl of diluted beads were mixed with 20 µl of mCherry tagged binding partner at a
627 concentration of 1.5 µM (0.5 µl bead slurry and 1 µM binding partner final concentrations)
628 with or without competitor, as stated in the relative experiment. The mixture was transferred
629 to a black, glass bottom, 384-well plate (Greiner Bio-One) and incubated for 30-60 min at
630 RT.

631 Imaging was performed with either a Zeiss LSM700 confocal microscope with 20 X
632 magnification or with a Zeiss LSM800 confocal microscope with 10 X magnification.

633 **Quantification of microscopy-based protein-protein interaction assays**

634 From images acquired from a Zeiss LSM700 confocal microscope, the quantification of
635 fluorescence was performed in ImageJ [69] by drawing a line across each bead and taking
636 the maximum gray value along the line. The maximum gray value for any given pixel
637 represents the fluorescence intensity.

638 For images acquired from a Zeiss LSM800 confocal microscope, we used a custom Fiji
639 Macro. Within this workflow a pretrained model was created for the deep learning application
640 "Stardist" (https://imagej.net/plugins/stardist) [71]. This model was based on a manually
641 annotated training set, using the fluorescently labelled beads as a basis for creating the
642 ground truth annotations, then performing the training on the brightfield channel. Out of focus
643 beads were rejected in this step and therefore excluded from the training. After applying the
644 deep learning-based segmentation, the regions were reduced to a ring around the edge of
645 the beads. Beads on image borders were excluded from the analysis. In the end, the mean
646 fluorescent intensities were exported out and used for quantification.

647 For each method, the fluorescence intensity was normalized against the mean of the control

bioRxiv preprint doi: https://doi.org/10.1101/2022.04.26.489478; this version posted April 26, 2022. The copyright holder for this preprint (which was not certified by peer review) is the author/funder, who has granted bioRxiv a license to display the preprint in perpetuity. It is made available under aCC-BY 4.0 International license.

648 condition.

649 Fiji macro and agarose bead model for automatic quantification are available in
650 Supplementary Data 3.

651 **Mass Spectrometry Measurements**

652 Proteins were buffer exchanged into ammonium acetate using BioRad Micro Bio-Spin 6
653 Columns. Native mass spectrometry experiments were carried out on a Synapt G2Si
654 instrument (Waters, Manchester, UK) with a nanoelectrospray ionization source (nESI).
655 Mass calibration was performed by a separate infusion of NaI cluster ions. Solutions were
656 ionized from a thin-walled borosilicate glass capillary (i.d. 0.78 mm, o.d. 1.0 mm, Sutter
657 Instrument Co., Novato, CA, USA) pulled in-house to nESI tip with a Flaming/Brown
658 micropipette puller (Sutter Instrument Co., Novato, CA, USA). A potential of 0.8 kV was
659 applied to the solution via a thin platinum wire (diameter 0.125 mm, Goodfellow, Huntingdon,
660 UK). The following instrument parameters were used: capillary voltage 0.8 kV, sample cone
661 voltage 40 V, source offset 60 V, source temperature 40 °C, trap collision energy 4.0 V, trap
662 gas 3 mL/min. Data were processed using Masslynx V4.2 and OriginPro 2021.

663 **NMR spectroscopy**

664 All NMR spectroscopy measurements were performed using Bruker AVIII 600MHz or
665 Avance 800MHz spectrometers at 25ºC. The data were processed using TopSpin 3.2
666 (Bruker) and NMRPipe [72] and analysed using CcpNmr Analysis [73].

667 Sequence specific backbone assignments of AtC53 IDR were achieved using 2D ^{1}H-^{15}N
668 HSQC, 3D HNCA, 3D CBCACONH, 3D HNCACB, 3D HNCO, 3D HNCACO including 70
669 residues of 75 non-proline residues (93%). NMR titrations were performed by adding
670 unlabelled protein (75-300 μM) to 100 μM of ^{15}N single-labelled protein in 50 mM sodium
671 phosphate (pH 7.0), 100 mM NaCl and 10% (v/v) D_2O and monitored by two-dimensional ^{1}H-
672 ^{15}N HSQC.

673 **Statistical analysis**

674 All statistical analysis was performed using R Statistical Software (version 4.1.2; R
675 Foundation for Statistical Computing, Vienna, Austria) [74]. Statistical significance of
676 differences between two experimental groups was assessed with a two-tailed unpaired two-
677 samples t-test if the two groups were normally distributed (Shapiro-Wilk test) and their
678 variances were equal (F-test). If the groups were normally distributed but the variances were
679 not equal a two-samples Welch t-test was performed. If the groups were not normally
680 distributed, an unpaired two-samples Wilcoxon test with continuity correction was performed.

bioRxiv preprint doi: https://doi.org/10.1101/2022.04.26.489478; this version posted April 26, 2022. The copyright holder for this preprint (which was not certified by peer review) is the author/funder, who has granted bioRxiv a license to display the preprint in perpetuity. It is made available under aCC-BY 4.0 International license.

681 Differences between two data sets were considered significant at $p < 0.05$ (*); $p < 0.01$ (**);
682 $p<0.001$ (***). P value > 0.05 (ns, not significant).

683

bioRxiv preprint doi: https://doi.org/10.1101/2022.04.26.489478; this version posted April 26, 2022. The copyright holder for this preprint (which was not certified by peer review) is the author/funder, who has granted bioRxiv a license to display the preprint in perpetuity. It is made available under aCC-BY 4.0 International license.

MATERIALS

Reagent or Resource	Source or Reference	Identifier	Additional information
Experimental Model Organisms			
Arabidopsis thaliana: wt		Col-0	
Chlamydomonas reinhardtii: wt	Zhang R., et al. 2014 The Plant Cell.	CC-4533	
Chlamydomonas reinhardtii: uba5	Li et al. 2019 Nature Genetics	Cre13.g582350	LMJ.RY0402.221917
Chlamydomonas reinhardtii: ufl1	Li et al. 2019 Nature Genetics	Cre16.g686650	LMJ.RY0402.223798
Chlamydomonas reinhardtii: ire1	Li et al. 2019 Nature Genetics	Cre08.g371052	LMJ.RY0402.122895
Arabidopsis thaliana: c53	Stephani, Picchianti, et al. 2020 eLife	At5g06830	CRISPR/Cas9
Arabidopsis thaliana: pUbi::C53-mCherry x GFP-ATG8A/*c53*	This study		BASTA/Alli-YFP
Arabidopsis thaliana: pUbi::C53$^{sAIM(W276A, W287A, Y304A, W335A)}$-mCherry x GFP-ATG8A/*c53*	This study		BASTA/Alli-YFP
Arabidopsis thaliana: pUbi::C53$^{cAIM(IDWD274WDDI, IDWD285WDDI, IDWD333WDDI)}$-mCherry x GFP-ATG8A/*c53*	This study		BASTA/Alli-YFP
Arabidopsis thaliana: Arabidopsis thaliana: pUbi::C53-GFP x *c53*	Stephani, Picchianti, et al. 2020 eLife		Alli-YFP
Arabidopsis thaliana: pUbi::C53$^{sAIM(W276A, W287A, Y304A, W335A)}$-GFP x *c53*	Stephani, Picchianti, et al. 2020 eLife		Alli-YFP
Arabidopsis thaliana: pUbi::C53$^{cAIM(IDWD274WDDI, IDWD285WDDI, IDWD333WDDI)}$-GFP x *c53*	This study		Alli-YFP
Oligonucleotides			
Chlamydomonas Reinhardtii: E3_P1			AGAGCTCCTGCATACCCTGA
Chlamydomonas Reinhardtii: E3_E1_SR			CCGAGGAGAAACTGGCCTT
Chlamydomonas Reinhardtii: E3_E1_oMJ			CAGGCCATGTGAGAGTTTGC
Chlamydomonas Reinhardtii: E3_P2			CTCCTCAATGAGTGTGGCAA
Chlamydomonas Reinhardtii: E1_P2			CACACGGACATGACTGGAAC
Chlamydomonas Reinhardtii: E1_P1			AGAGTTACGGCCGCAGATT

bioRxiv preprint doi: https://doi.org/10.1101/2022.04.26.489478; this version posted April 26, 2022. The copyright holder for this preprint (which was not certified by peer review) is the author/funder, who has granted bioRxiv a license to display the preprint in perpetuity. It is made available under aCC-BY 4.0 International license.

Bacterial Strains	
E. coli: DH5α	In-house facility
E. coli: Rosetta2 (DE3) pLysS	In-house facility
A. tumefaciens: GV3101 (pSoup)	In-house facility
Recombinant DNA	
E. coli: Destination (expression) vector	Stephani, Picchianti, et al. 2020 eLife
E. coli: GST-ATG8A	Stephani, Picchianti, et al. 2020 eLife
E. coli: GST-ATG8A$^{LDS(YL50AA)}$	Stephani, Picchianti, et al. 2020 eLife
E. coli: GST-GABARAP	Stephani, Picchianti, et al. 2020 eLife
E. coli: GST-CrATG8	This study
E. coli: GST-CrUFM1	This study
E. coli: HIS6-CrC53	This study
E. coli: MBP-CrC53	This study
E. coli: GST-AtUFM1	Stephani, Picchianti, et al. 2020 eLife
E. coli: GST-HsUFM1	This study
E. coli: MBP-AtC53	Stephani, Picchianti, et al. 2020 eLife
E. coli: MBP-AtC53$^{IDR(239\text{-}372)}$	Stephani, Picchianti, et al. 2020 eLife
E. coli: MBP-AtC53$^{\Delta IDR(1\text{-}239,(KGSGSTSGSG)2,373\text{-}549)}$	Stephani, Picchianti, et al. 2020 eLife
E. coli: MBP-HsC53	Stephani, Picchianti, et al. 2020 eLife
E. coli: MBP-HsC53$^{IDR(263\text{-}316)}$	Stephani, Picchianti, et al. 2020 eLife
E. coli: MBP-HsC53$^{\Delta IDR(1\text{-}262,\ (KGSGSTSGSG),317\text{-}506)}$	Stephani, Picchianti, et al. 2020 eLife
E. coli: MBP-AtC53$^{1A\ (W276A)}$	Stephani, Picchianti, et al. 2020 eLife
E. coli: MBP-AtC53$^{2A\ (W287A)}$	Stephani, Picchianti, et al. 2020 eLife
E. coli: MBP-AtC53$^{3A\ (W335A)}$	Stephani, Picchianti, et al. 2020 eLife
E. coli: MBP-AtC53$^{12A\ (W276A,\ W287A)}$	Stephani,

bioRxiv preprint doi: https://doi.org/10.1101/2022.04.26.489478; this version posted April 26, 2022. The copyright holder for this preprint (which was not certified by peer review) is the author/funder, who has granted bioRxiv a license to display the preprint in perpetuity. It is made available under aCC-BY 4.0 International license.

	Picchianti, et al. 2020 eLife
E. coli: MBP-AtC53$^{13A\ (W276A,\ W335A)}$	Stephani, Picchianti, et al. 2020 eLife
E. coli: MBP-AtC53$^{23A\ (W287A,\ W335A)}$	Stephani, Picchianti, et al. 2020 eLife
E. coli: MBP-AtC53$^{123A(W276A,\ W287A,\ W335A)}$	Stephani, Picchianti, et al. 2020 eLife
E. coli: MBP-AtC53$^{sAIM(Y304A,\ W276A,\ W287A,\ W335A)}$	Stephani, Picchianti, et al. 2020 eLife
E. coli: MBP-HsC53$^{sAIM(W269A,\ W294A,\ W312A)}$	Stephani, Picchianti, et al. 2020 eLife
E. coli: MBP	Stephani, Picchianti, et al. 2020 eLife
E. coli: HIS6-GABARAP	Stephani, Picchianti, et al. 2020 eLife
E. coli: HIS6-AtC53	Stephani, Picchianti, et al. 2020 eLife
E. coli: mCh-AtC53$^{sAIM\ (Y304A,\ W276A,\ W287A,\ W335A)}$	This study
E. coli: mCh-HsC53$^{sAIM(W269A,\ W294A,\ W312A)}$	This study
E. coli: mCh-AtC53	
E. coli: mCh-HsC53	
E. coli: GST	Stephani, Picchianti, et al. 2020 eLife
E. coli: mCherry	This study
E. coli: MBP- *E. coli:* AtC53$^{cAIM(IDWD274WDDI,\ IDWD285WDDI,\ IDWD333WDDI)}$	This study
E. coli: MBP-HsC53$^{cAIM(IDWG267WDGI,\ IDWG292WDGI,\ IDWG310WDGI)}$	This study
E. coli: mCh-AtC53$^{cAIM(IDWD274WDDI,\ IDWD285WDDI,\ IDWD333WDDI)}$	This study
E. coli: mCh-HsC53$^{cAIM(IDWG267WDGI,\ IDWG292WDGI,\ IDWG310WDGI)}$	This study
E. coli: HIS6-HsC53	Stephani, Picchianti, et al. 2020 eLife
E. coli: HIS6-HsUFM1	Stephani, Picchianti, et al. 2020 eLife
E. coli: HIS6-AtUFM1	Stephani, Picchianti, et al. 2020 eLife
E. coli: MBP-PfC53	This study
E. coli: MBP-AcC53	This study

bioRxiv preprint doi: https://doi.org/10.1101/2022.04.26.489478; this version posted April 26, 2022. The copyright holder for this preprint (which was not certified by peer review) is the author/funder, who has granted bioRxiv a license to display the preprint in perpetuity. It is made available under aCC-BY 4.0 International license.

E. coli: HIS6-MBP-3C-AtC53 IDR $^{(264\text{-}341)}$	This study		
E. coli: HIS6-MBP-3C-AtC53 IDR$^{1A\ (W276A)\ (264\text{-}341)}$	This study		
E. coli: HIS6-MBP-3C-AtC53 IDR$^{2A\ (W287A)\ (264\text{-}341)}$	This study		
E. coli: HIS6-3C-GABARAP	This study		
E. coli: HIS6-3C-ATG8A	This study		
E. coli: HIS6-3C-AtUFM1	This study		
E. coli: HIS6-3C-HsUFM1	This study		
E. coli: HIS6-MBP-3C-HsC53 IDR $^{(263\text{-}316)}$	This study		
pUbi::C53$^{sAIM(W276A,\ W287A,\ Y304A,\ W335A)}$-mCherry	This study		
pUbi::C53$^{cAIM(IDWD274WDDI,\ IDWD285WDDI,\ IDWD333WDDI)}$-mCherry	This study		
pUbi::C53$^{cAIM(IDWD274WDDI,\ IDWD285WDDI,\ IDWD333WDDI)}$-GFP	This study		
pUbi::C53-mCherry	Stephani, Picchianti, et al. 2020 eLife		
pUbi::C53-GFP	Stephani, Picchianti, et al. 2020 eLife		
pUbi::C53$^{sAIM(W276A,\ W287A,\ Y304A,\ W335A)}$-GFP	Stephani, Picchianti, et al. 2020 eLife		
Peptides			
cAIM	Synthetized *in house*		EPLDFDWEI VLEEEM
cAIM mutant	Synthetized *in house*		EPLDFDAEI ALEEEM
AtUBA5 LIR	Synthetized *in house*		GPLHDDNE WNISVVDD
HsUBA5 LIR	Synthetized *in house*		EIIHEDNEW GIELVSE
Antibodies			
Anti-Rabbit IgG HRP-Conjugate	Biorad	1706515	Host: goat Working dilution: 1:10000
Anti-Mouse IgG-HRP Conjugate	Biorad	1706516	Host: goat Working dilution: 1:10000
mCherry	Abcam	ab167453	Host: rabbit Working dilution: 1:5000
GST HRP Conjugate	GE Healthcare	RPN1236	Host: goat Working dilution: 1:1000
GFP	Invitrogen	A11122	Host: rabbit Working dilution:

bioRxiv preprint doi: https://doi.org/10.1101/2022.04.26.489478; this version posted April 26, 2022. The copyright holder for this preprint (which was not certified by peer review) is the author/funder, who has granted bioRxiv a license to display the preprint in perpetuity. It is made available under aCC-BY 4.0 International license.

			1:3000
GFP	Roche	1181446 0001	Host: mouse Working dilution: 1:3000
MBP	Sigma Aldrich	M1321-200UL	Host: mouse Working dilution: 1:3000
ATG8A	Agrisera	AS14 2811	Host: rabbit Working dilution: 1:1000
C53	Stephani, Picchianti, et al. 2020 eLife	-	Host: rabbit Working dilution: 1:5000
UFM1	Abcam	Ab10930 5	Host: rabbit Working dilution: 1:3000
Inhibitors and Drugs			
Tunicamycin	SCBT	sc-3506	
DTT	Sigma Aldrich	43815	
Concanamycin-A (conA)	Santa Cruz	sc-202111A	
Media and Supplements			
gamborg B5 vitamin mixture 1000X	Duchefa	G0415.0 250	
gamborg B5 medium (microsalt mixture)	Duchefa	M0302.0 025	
gamborg B5 medium (including vitamins)	Duchefa	G0210.0 010	
gamborg B5 medium (basal salt mixture)	Duchefa	G0209.0 050	
Murashige & Skoog vitamin mixture 1000X	Duchefa	M0409.0 250	
Murashige & Skoog micro salt mixture	Duchefa	M0301.0 050	
Murashige & Skoog macro salt mixture	Duchefa	M0305.0 050	
Murshige & Skoog Basal salt mixture with MES	Duchefa	M0254.0 050	
Murashige & Skoog without nitrogen	Caisson labs		
MES monohydrate	Applichem	A1074	
Puromycin	Sigma Aldrich	P8833	
L-Glutamine	Sigma Aldrich	G7513	
M9 Minimal media	In-house facility		
Ammonium-^{15}N chloride	Sigma Aldrich	39466-62-1	
D-Glucose (U-13C6, 99%)	Cambridge Isotope Laboratories, Inc.	110187-42-3	

bioRxiv preprint doi: https://doi.org/10.1101/2022.04.26.489478; this version posted April 26, 2022. The copyright holder for this preprint (which was not certified by peer review) is the author/funder, who has granted bioRxiv a license to display the preprint in perpetuity. It is made available under aCC-BY 4.0 International license.

Thamine hydrochloride	Sigma Aldrich	T1270	
Biotin	Sigma Aldrich	B4639	
Choline chloride	Alfa Aesar	A15828	
Folic acid	Acros Organics	21663	
Niacinamide	Sigma Aldrich	N3376	
D-Pantothenic acid hemicalcium salt	Sigma Aldrich	P2250	
Pyridoxal hydrochloride	Alfa Aesar	A17855	
(-)-Riboflavin	Sigma Aldrich	R4500	
Ethylenedinitrilotetraacetic acid disodium salt dihydrate	Merck	108454	
Iron (III) chloride hexahydrate $Fe(III)Cl_3 \cdot 6H_2O$	Merck	103943	
Zinc chloride $ZnCl_2$	Merck	108816	
Copper (II) chloride dihydrate $Cu(II)Cl_2 \cdot 2H_2O$	Sigma Aldrich	221783	
Cobalt (II) chloride hexahydrate $Co(II)Cl_2 \cdot 6H_2O$	Sigma Aldrich	S2644	
Boric acid	Sigma Aldrich	B6768	
Manganese (II) chloride tetrahydrate $Mn(II)Cl_2 \cdot 4H_2O$	Sigma Aldrich	M3634	
Matrices for protein purification and immuno-precipitations			
GFP-Trap	Chromotek	Gta-20	
Glutathion Sepharose 4 B	GE Healthcare	17-5132-01	
Pierce™ Glutathione Magnetic Agarose Beads	Thermo Scientific™	78601	
HisTrap FF 5 ml	GE Healthcare	17525501	
HisTrap FF 1 ml	GE Healthcare	17531901	
Resource Q 6 ml	GE Healthcare	17117901	
Resource S 6 ml	GE Healthcare	17118001	
HiPrep 26/10 Desalting	GE Healthcare	17508701	
HiLoad 16/600 Superdex 75 pg	GE Healthcare	28989333	
HiLoad 16/600 Superdex 200 pg	GE Healthcare	28989335	
GFP-Trap Magnetic Agarose	Chromotek	Gtma-20	
Protein A Agarose	Sigma	P2545	
Software			
CLC main work bench 7	Qiagen		Cloning
Zen Software	Carl Zeiss		Microscopy
Image J (Fiji)	NIH		Image Quantification
Image Lab	BioRad		Western Blot Analysis
iBright analysis software	Invitrogen		Western Blot Analysis

bioRxiv preprint doi: https://doi.org/10.1101/2022.04.26.489478; this version posted April 26, 2022. The copyright holder for this preprint (which was not certified by peer review) is the author/funder, who has granted bioRxiv a license to display the preprint in perpetuity. It is made available under aCC-BY 4.0 International license.

Adobe Illustrator 2022	Adobe Inc.	Graphics editing
RStudio 2021.09.2+382 "Ghost Orchid" Release; R version 4.1.2	RStudio; The R Foundation for Statistical Computing	Graph plotting, Statistical analysis
TopSpin3.2	Bruker	NMR software
CcpNmr3.0	Continuum Analytics, Inc.	NMR Analysis software

bioRxiv preprint doi: https://doi.org/10.1101/2022.04.26.489478; this version posted April 26, 2022. The copyright holder for this preprint (which was not certified by peer review) is the author/funder, who has granted bioRxiv a license to display the preprint in perpetuity. It is made available under aCC-BY 4.0 International license.

References

1. Pohl C, Dikic I (2019) Cellular quality control by the ubiquitin-proteasome system and autophagy. Science 366:818–822. https://doi.org/10.1126/science.aax3769

2. Sun Z, Brodsky JL (2019) Protein quality control in the secretory pathway. J Cell Biol 218:3171–3187. https://doi.org/10.1083/jcb.201906047

3. Karagöz GE, Acosta-Alvear D, Walter P (2019) The Unfolded Protein Response: Detecting and Responding to Fluctuations in the Protein-Folding Capacity of the Endoplasmic Reticulum. Cold Spring Harb Perspect Biol 11:. https://doi.org/10.1101/cshperspect.a033886

4. Kirkin V, Rogov VV (2019) A Diversity of Selective Autophagy Receptors Determines the Specificity of the Autophagy Pathway. Molecular Cell 76:268–285. https://doi.org/10.1016/j.molcel.2019.09.005

5. Dikic I (2017) Proteasomal and Autophagic Degradation Systems. Annu Rev Biochem 86:193–224. https://doi.org/10.1146/annurev-biochem-061516-044908

6. Klionsky DJ, Petroni G, Amaravadi RK, et al (2021) Autophagy in major human diseases. EMBO J 40:e108863. https://doi.org/10.15252/embj.2021108863

7. Stephani M, Dagdas Y (2020) Plant Selective Autophagy—Still an Uncharted Territory With a Lot of Hidden Gems. J Mol Biol 432:. https://doi.org/10.1016/j.jmb.2019.06.028

8. Marshall RS, Vierstra RD (2018) Autophagy: The Master of Bulk and Selective Recycling. Annu Rev Plant Biol 69:173–208. https://doi.org/10.1146/annurev-arplant-042817-040606

9. Mizushima N (2018) A brief history of autophagy from cell biology to physiology and disease. Nat Cell Biol 20:521–527. https://doi.org/10.1038/s41556-018-0092-5

10. Dikic I, Elazar Z (2018) Mechanism and medical implications of mammalian autophagy. Nat Rev Mol Cell Biol 19:349–364. https://doi.org/10.1038/s41580-018-0003-4

11. Kirkin V (2020) History of the Selective Autophagy Research: How Did It Begin and Where Does It Stand Today? Journal of Molecular Biology 432:3–27. https://doi.org/10.1016/j.jmb.2019.05.010

12. Birgisdottir ÅB, Lamark T, Johansen T (2013) The LIR motif - crucial for selective autophagy. Journal of Cell Science 126:3237–3247. https://doi.org/10.1242/jcs.126128

13. Johansen T, Lamark T (2020) Selective Autophagy: ATG8 Family Proteins, LIR Motifs and Cargo Receptors. Journal of Molecular Biology 432:80–103. https://doi.org/10.1016/j.jmb.2019.07.016

14. Stephani M, Picchianti L, Gajic A, et al (2020) A cross-kingdom conserved er-phagy receptor maintains endoplasmic reticulum homeostasis during stress. eLife 9:1–105. https://doi.org/10.7554/ELIFE.58396

15. Liang JR, Lingeman E, Luong T, et al (2020) A Genome-wide ER-phagy Screen Highlights Key Roles of Mitochondrial Metabolism and ER-Resident UFMylation. Cell 180:1160-1177.e20. https://doi.org/10.1016/j.cell.2020.02.017

bioRxiv preprint doi: https://doi.org/10.1101/2022.04.26.489478; this version posted April 26, 2022. The copyright holder for this preprint (which was not certified by peer review) is the author/funder, who has granted bioRxiv a license to display the preprint in perpetuity. It is made available under aCC-BY 4.0 International license.

16. Daniel J, Liebau E (2014) The Ufm1 Cascade. Cells 3:627–638. https://doi.org/10.3390/cells3020627

17. Banerjee S, Kumar M, Wiener R (2020) Decrypting UFMylation: How Proteins Are Modified with UFM1. Biomolecules 10:. https://doi.org/10.3390/biom10101442

18. Oweis W, Padala P, Hassouna F, et al (2016) Trans-Binding Mechanism of Ubiquitin-like Protein Activation Revealed by a UBA5-UFM1 Complex. Cell Reports 16:3113–3120. https://doi.org/10.1016/j.celrep.2016.08.067

19. Kumar M, Padala P, Fahoum J, et al (2021) Structural basis for UFM1 transfer from UBA5 to UFC1. Nature Communications 12:1–13. https://doi.org/10.1038/s41467-021-25994-6

20. Zhou J, Liang Q, Dong M, et al (2022) Optimized protocol to detect protein UFMylation in cells and in vitro via immunoblotting. STAR Protocols 3:101074. https://doi.org/10.1016/j.xpro.2021.101074

21. Peter JJ, Magnussen HM, DaRosa PA, et al (2022) Non-canonical scaffold-type ligase complex mediates protein UFMylation. bioRxiv 2022.01.31.478489

22. Walczak CP, Leto DE, Zhang L, et al (2019) Ribosomal protein RPL26 is the principal target of UFMylation. Proc Natl Acad Sci U S A 116:1299–1308. https://doi.org/10.1073/pnas.1816202116

23. Wang L, Xu Y, Rogers H, et al (2020) UFMylation of RPL26 links translocation-associated quality control to endoplasmic reticulum protein homeostasis. Cell Res 30:5–20. https://doi.org/10.1038/s41422-019-0236-6

24. Wolf YI, Koonin EV (2013) Genome reduction as the dominant mode of evolution. BioEssays 35:829–837. https://doi.org/10.1002/bies.201300037

25. Ashkenazy H, Abadi S, Martz E, et al (2016) ConSurf 2016: an improved methodology to estimate and visualize evolutionary conservation in macromolecules. Nucleic Acids Res 44:W344-50. https://doi.org/10.1093/nar/gkw408

26. Habisov S, Huber J, Ichimura Y, et al (2016) Structural and Functional Analysis of a Novel Interaction Motif within UFM1-activating Enzyme 5 (UBA5) Required for Binding to Ubiquitin-like Proteins and Ufmylation. J Biol Chem 291:9025–9041. https://doi.org/10.1074/jbc.M116.715474

27. Huber J, Obata M, Gruber J, et al (2020) An atypical LIR motif within UBA5 (ubiquitin like modifier activating enzyme 5) interacts with GABARAP proteins and mediates membrane localization of UBA5. Autophagy 16:256–270. https://doi.org/10.1080/15548627.2019.1606637

28. Padala P, Oweis W, Mashahreh B, et al (2017) Novel insights into the interaction of UBA5 with UFM1 via a UFM1-interacting sequence. Scientific Reports 7:1–12. https://doi.org/10.1038/s41598-017-00610-0

29. Turco E, Witt M, Abert C, et al (2019) FIP200 Claw Domain Binding to p62 Promotes Autophagosome Formation at Ubiquitin Condensates. Mol Cell 74:330-346.e11. https://doi.org/10.1016/j.molcel.2019.01.035

bioRxiv preprint doi: https://doi.org/10.1101/2022.04.26.489478; this version posted April 26, 2022. The copyright holder for this preprint (which was not certified by peer review) is the author/funder, who has granted bioRxiv a license to display the preprint in perpetuity. It is made available under aCC-BY 4.0 International license.

30. Cox M, Dekker N, Boelens R, et al (1993) NMR studies of the POU-specific DNA-binding domain of Oct-1: Sequential proton and nitrogen-15 assignments and secondary structure. Biochemistry 32:6032–6040. https://doi.org/10.1021/bi00074a014

31. Sette M, Spurio R, van Tilborg P, et al (1999) Identification of the ribosome binding sites of translation initiation factor IF3 by multidimensional heteronuclear NMR spectroscopy. RNA 5:82–92. https://doi.org/10.1017/s1355838299981487

32. Wüthrich K (2003) NMR studies of structure and function of biological macromolecules (Nobel Lecture). J Biomol NMR 27:13–39. https://doi.org/10.1023/a:1024733922459

33. Zuiderweg ERP (2002) Mapping protein-protein interactions in solution by NMR spectroscopy. Biochemistry 41:1–7. https://doi.org/10.1021/bi011870b

34. Sasakawa H, Sakata E, Yamaguchi Y, et al (2006) Solution structure and dynamics of Ufm1, a ubiquitin-fold modifier 1. Biochem Biophys Res Commun 343:21–26. https://doi.org/10.1016/j.bbrc.2006.02.107

35. Kouno T, Miura K, Kanematsu T, et al (2002) Letter to the Editor: 1H, 13C and 15N resonance assignments of GABARAP, GABAA receptor associated protein. Journal of Biomolecular NMR 22:97–98. https://doi.org/10.1023/A:1013884402033

36. Noda NN, Ohsumi Y, Inagaki F (2010) Atg8-family interacting motif crucial for selective autophagy. FEBS Letters 584:1379–1385. https://doi.org/10.1016/j.febslet.2010.01.018

37. Zientara-Rytter K, Subramani S (2020) Mechanistic Insights into the Role of Atg11 in Selective Autophagy. J Mol Biol 432:104–122. https://doi.org/10.1016/j.jmb.2019.06.017

38. Turco E, Fracchiolla D, Martens S (2020) Recruitment and Activation of the ULK1/Atg1 Kinase Complex in Selective Autophagy. J Mol Biol 432:123–134. https://doi.org/10.1016/j.jmb.2019.07.027

39. Brandizzi F (2021) Maintaining the structural and functional homeostasis of the plant endoplasmic reticulum. Dev Cell. https://doi.org/10.1016/j.devcel.2021.02.008

40. Gerakis Y, Quintero M, Li H, Hetz C (2019) The UFMylation System in Proteostasis and Beyond. Trends Cell Biol 29:974–986. https://doi.org/10.1016/j.tcb.2019.09.005

41. Eck F, Kaulich M, Behrends C ACSL3 is a novel GABARAPL2 interactor that links ufmylation and lipid droplet biogenesis

42. Liu J, Guan D, Dong M, et al (2020) UFMylation maintains tumour suppressor p53 stability by antagonizing its ubiquitination. Nat Cell Biol 22:1056–1063. https://doi.org/10.1038/s41556-020-0559-z

43. Lee L, Perez Oliva AB, Martinez-Balsalobre E, et al (2021) UFMylation of MRE11 is essential for telomere length maintenance and hematopoietic stem cell survival. Sci Adv 7:eabc7371. https://doi.org/10.1126/sciadv.abc7371

44. Qin B, Yu J, Nowsheen S, et al (2019) UFL1 promotes histone H4 ufmylation and ATM activation. Nat Commun 10:1242. https://doi.org/10.1038/s41467-019-09175-0

45. Kulsuptrakul J, Wang R, Meyers NL, et al (2020) A genome-wide CRISPR screen identifies UFMylation and TRAMP-like complexes as host factors required for hepatitis A virus infection. Cold Spring Harbor Laboratory 2019.12.15.877100

bioRxiv preprint doi: https://doi.org/10.1101/2022.04.26.489478; this version posted April 26, 2022. The copyright holder for this preprint (which was not certified by peer review) is the author/funder, who has granted bioRxiv a license to display the preprint in perpetuity. It is made available under aCC-BY 4.0 International license.

46. UFMylation inhibits the proinflammatory capacity of interferon-γ–activated macrophages. In: PNAS. https://www.pnas.org/content/pnas/118/1/e2011763118. Accessed 4 Apr 2022

47. Tsaban T, Stupp D, Sherill-Rofe D, et al (2021) CladeOScope: Functional interactions through the prism of clade-wise co-evolution. NAR Genomics and Bioinformatics 3:1–13. https://doi.org/10.1093/nargab/lqab024

48. Buchfink B, Xie C, Huson DH (2014) Fast and sensitive protein alignment using DIAMOND. Nature Methods 12:59–60. https://doi.org/10.1038/nmeth.3176

49. Katoh K, Standley DM (2013) MAFFT multiple sequence alignment software version 7: Improvements in performance and usability. Molecular Biology and Evolution 30:772–780. https://doi.org/10.1093/molbev/mst010

50. Capella-Gutiérrez S, Silla-Martínez JM, Gabaldón T (2009) trimAl: A tool for automated alignment trimming in large-scale phylogenetic analyses. Bioinformatics 25:1972–1973. https://doi.org/10.1093/bioinformatics/btp348

51. Minh BQ, Schmidt HA, Chernomor O, et al (2020) IQ-TREE 2: New models and efficient methods for phylogenetic inference in the genomic era. Molecular Biology and Evolution 37:1530–1534. https://doi.org/10.1093/molbev/msaa015

52. Boeckmann B, Bairoch A, Apweiler R, et al (2003) The SWISS-PROT protein knowledgebase and its supplement TrEMBL in 2003. Nucleic Acids Research 31:365–370. https://doi.org/10.1093/nar/gkg095

53. El-Gebali S, Mistry J, Bateman A, et al (2019) The Pfam protein families database in 2019. Nucleic Acids Research 47:D427–D432. https://doi.org/10.1093/nar/gky995

54. Rambaut A (2012) FigTree, a graphical viewer of phylogenetic trees. See http://tree.bio.ed.ac.uk/software/figtree

55. Rozewicki J, Li S, Amada KM, et al (2019) MAFFT-DASH: Integrated protein sequence and structural alignment. Nucleic Acids Research 47:W5–W10. https://doi.org/10.1093/nar/gkz342

56. Mistry J, Finn RD, Eddy SR, et al (2013) Challenges in homology search: HMMER3 and convergent evolution of coiled-coil regions. Nucleic Acids Research 41:e121. https://doi.org/10.1093/nar/gkt263

57. Slater GSC, Birney E (2005) Automated generation of heuristics for biological sequence comparison. BMC Bioinformatics 6:31. https://doi.org/10.1186/1471-2105-6-31

58. Letunic I, Bork P (2021) Interactive tree of life (iTOL) v5: An online tool for phylogenetic tree display and annotation. Nucleic Acids Research 49:W293–W296. https://doi.org/10.1093/nar/gkab301

59. Burki F, Roger AJ, Brown MW, Simpson AGB (2020) The new tree of eukaryotes. Trends in Ecology and Evolution 35:43–55. https://doi.org/10.1016/j.tree.2019.08.008

60. Federhen S (2012) The NCBI Taxonomy database. Nucleic Acids Research 40:136–143. https://doi.org/10.1093/nar/gkr1178

61. Edgar RC (2004) MUSCLE: A multiple sequence alignment method with reduced time and space complexity. BMC Bioinformatics 5:113. https://doi.org/10.1186/1471-2105-5-113

bioRxiv preprint doi: https://doi.org/10.1101/2022.04.26.489478; this version posted April 26, 2022. The copyright holder for this preprint (which was not certified by peer review) is the author/funder, who has granted bioRxiv a license to display the preprint in perpetuity. It is made available under aCC-BY 4.0 International license.

62. Larsson A (2014) AliView: a fast and lightweight alignment viewer and editor for large datasets. Bioinformatics 30:3276–3278

63. Kalyaanamoorthy S, Minh BQ, Wong TKF, et al (2017) ModelFinder: Fast model selection for accurate phylogenetic estimates. Nature Methods 14:587–589. https://doi.org/10.1038/nmeth.4285

64. Penev PI, Alvarez-Carreño C, Smith E, et al (2021) TwinCons: Conservation score for uncovering deep sequence similarity and divergence. PLoS Computational Biology 17:e1009541. https://doi.org/10.1371/journal.pcbi.1009541

65. Wheeler TJ, Clements J, Finn RD (2014) Skylign: A tool for creating informative, interactive logos representing sequence alignments and profile hidden Markov models. BMC Bioinformatics 15:7. https://doi.org/10.1186/1471-2105-15-7

66. Lampropoulos A, Sutikovic Z, Wenzl C, et al (2013) GreenGate---a novel, versatile, and efficient cloning system for plant transgenesis. PLoS One 8:e83043. https://doi.org/10.1371/journal.pone.0083043

67. Perlaza K, Toutkoushian H, Boone M, et al (2019) The mars1 kinase confers photoprotection through signaling in the chloroplast unfolded protein response. eLife 8:1–36. https://doi.org/10.7554/eLife.49577

68. Bechtold N, Pelletier G (1998) In planta Agrobacterium-mediated transformation of adult Arabidopsis thaliana plants by vacuum infiltration. Methods in molecular biology (Clifton, NJ) 82:259–266. https://doi.org/10.1385/0-89603-391-0:259

69. Schindelin J, Arganda-Carreras I, Frise E, et al (2012) Fiji: an open-source platform for biological-image analysis. Nature methods 9:676–682. https://doi.org/10.1038/nmeth.2019

70. Marley J, Lu M, Bracken C (2001) A method for efficient isotopic labeling of recombinant proteins. Journal of biomolecular NMR 20:71–75. https://doi.org/10.1023/a:1011254402785

71. Schmidt U, Weigert M, Broaddus C, Myers G (2018) Cell detection with star-convex polygons. Lecture Notes in Computer Science (including subseries Lecture Notes in Artificial Intelligence and Lecture Notes in Bioinformatics) 11071 LNCS:265–273. https://doi.org/10.1007/978-3-030-00934-2_30

72. Delaglio F, Grzesiek S, Vuister GW, et al (1995) NMRPipe: a multidimensional spectral processing system based on UNIX pipes. Journal of biomolecular NMR 6:277–293. https://doi.org/10.1007/BF00197809

73. Skinner SP, Fogh RH, Boucher W, et al (2016) CcpNmr AnalysisAssign: a flexible platform for integrated NMR analysis. Journal of biomolecular NMR 66:111–124. https://doi.org/10.1007/s10858-016-0060-y

74. R Core Team (2021) R: A Language and Environment for Statistical Computing

bioRxiv preprint doi: https://doi.org/10.1101/2022.04.26.489478; this version posted April 26, 2022. The copyright holder for this preprint (which was not certified by peer review) is the author/funder, who has granted bioRxiv a license to display the preprint in perpetuity. It is made available under aCC-BY 4.0 International license.

Fig. 1

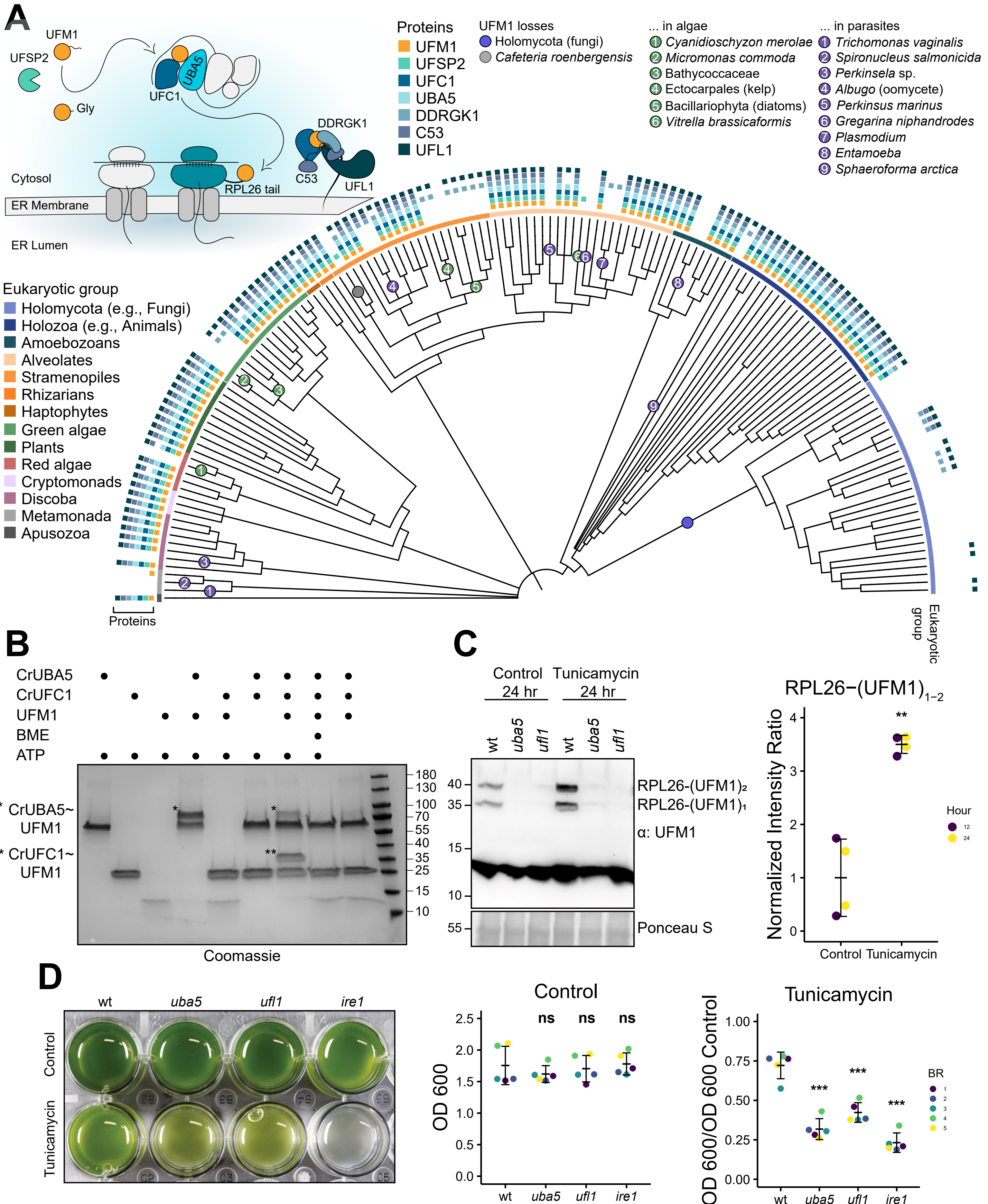

bioRxiv preprint doi: https://doi.org/10.1101/2022.04.26.489478; this version posted April 26, 2022. The copyright holder for this preprint (which was not certified by peer review) is the author/funder, who has granted bioRxiv a license to display the preprint in perpetuity. It is made available under aCC-BY 4.0 International license.

Figure 1. UFMylation did not evolve in multicellular eukaryotes.

(A) A eukaryotic phylogeny displaying the presence or absence of UFMylation proteins across diverse species. Protein presence is displayed at the tip of each tree and major eukaryotic taxonomic groups are denoted with a colored ribbon. Losses of UFM1 have been highlighted. A schematic diagram depicting UFMylation cascade and C53-receptor complex has been included for reference. See Fig. S1 for an expanded phylogeny, including species names. **(B) *Chlamydomonas reinhardtii* (Cr) UBA5 and UFC1 are active E1 and E2 enzymes**. SDS-PAGE analysis showing transfer of UFM1 to CrUBA5 and CrUFC1. The gels are run in non-reducing conditions except where otherwise specified. The presented gel is representative of two independent experiments. BME: β-mercaptoethanol; ATP: Adenosine triphosphate. **(C) RPL26 mono- and di-UFMylation is lost in *Chlamydomonas reinhardtii* (Cr) *uba5* and *ufl1* mutants**. Liquid TAP cultures were either left untreated (control) or treated for 24 hours with 200 ng/mL tunicamycin. Protein extracts were analyzed by immunoblotting with anti-UFM1 antibodies. Total proteins were analyzed by Ponceau S staining. 12 hours and 24 hours treatment replicates are shown in Fig. S3C. *Right Panel*, Quantification of UFMylated RPL26. Bars represent the mean (± SD) of 2 biological replicates. Two-tailed unpaired t-test with Welch correction was performed to analyze the differences between control and treated samples. **, p-value < 0.01. RPL26-$(UFM1)_1$: RPL26 mono-UFMylated; RPL26-$(UFM1)_2$: RPL26 di-UFMylated. **(D) *Chlamydomonas reinhardtii* (Cr) UFMylation pathway mutants are sensitive to ER stress triggered by tunicamycin**. Liquid TAP cultures of wild type (wt), *uba5, ufl1* and *ire1* mutants were either left untreated (control) or treated for 3 days with 200 ng/mL of tunicamycin. *Left panel,* representative images of control and treated liquid cultures taken 3-days after incubation. *Middle Panel,* optical density (OD) 600 (OD_{600}) quantification of each genetic background under control conditions. Bars represent the mean (± SD) of 5 biological replicates. Two-tailed unpaired t-tests were performed to analyze the differences between wild type and mutants. *Right Panel,* normalized OD_{600} quantification of each genetic background under tunicamycin treatment conditions. Bars represent the mean (± SD) of 5 biological replicates. Two-tailed unpaired t-tests were performed to analyze the differences between wild type and mutants. ns, p-value > 0.05; ***, p-value < 0.001. BR: Biological Replicate.

bioRxiv preprint doi: https://doi.org/10.1101/2022.04.26.489478; this version posted April 26, 2022. The copyright holder for this preprint (which was not certified by peer review) is the author/funder, who has granted bioRxiv a license to display the preprint in perpetuity. It is made available under aCC-BY 4.0 International license.

Fig. 2

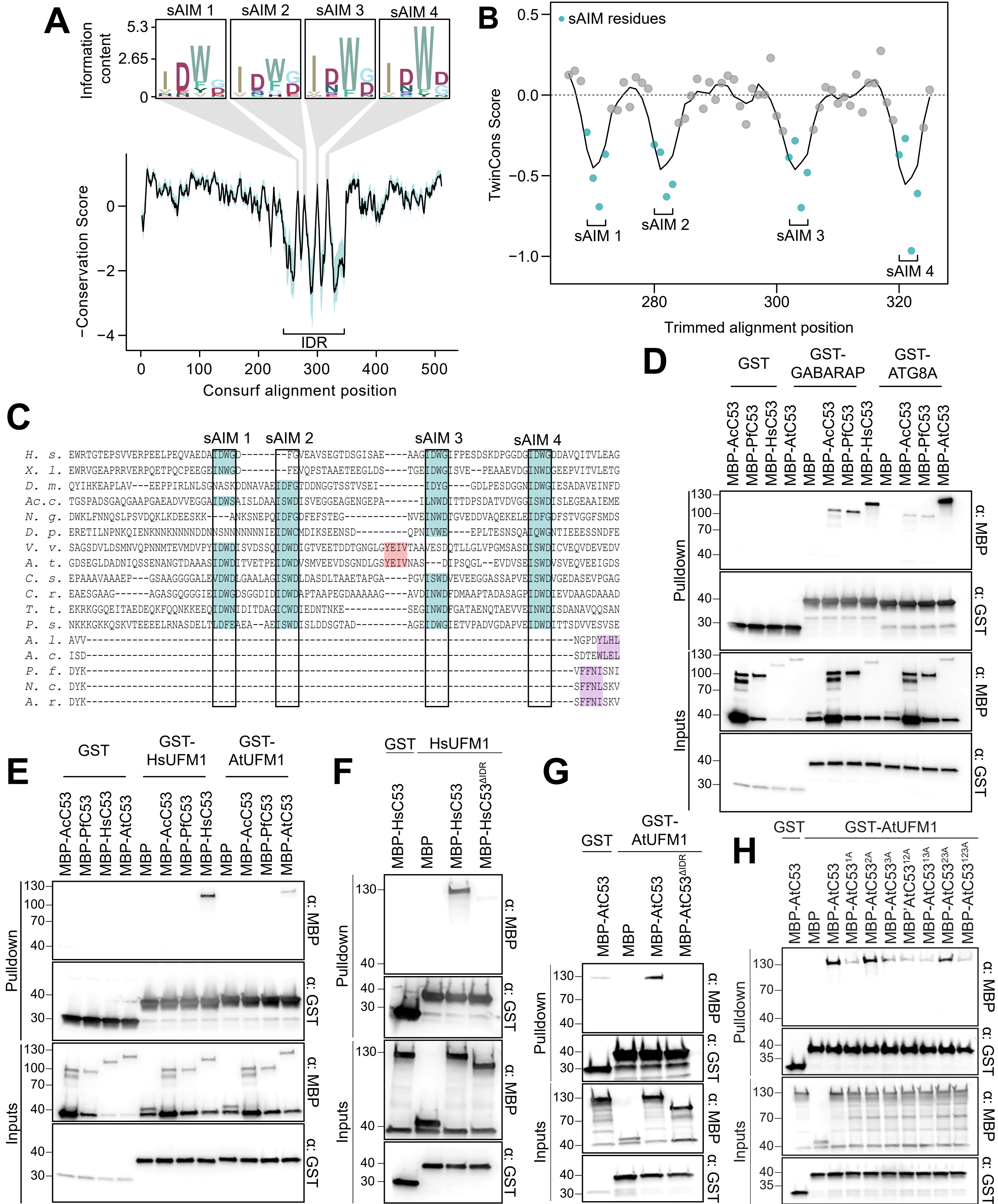

bioRxiv preprint doi: https://doi.org/10.1101/2022.04.26.489478; this version posted April 26, 2022. The copyright holder for this preprint (which was not certified by peer review) is the author/funder, who has granted bioRxiv a license to display the preprint in perpetuity. It is made available under aCC-BY 4.0 International license.

Figure 2. The sAIM sequences within C53 Intrinsically Disordered Region (IDR) are highly conserved and essential for UFM1 interaction.

(A) ConSurf conservation analysis of C53 from diverse eukaryotes. Conserved regions within the IDR (intrinsically disordered region) have been highlighted and supplemented with sequence logos. **(B) TwinCons analysis comparing the conservation and divergence of C53 among species with and without UFM1.** The four regions corresponding to the sAIMs have been highlighted. Negative values reflect divergent signature regions between the two species groups. (**C) A trimmed multiple sequence alignment depicting the conservation of the sAIMs.** The four sAIMs and cAIMs in plants and UFM1-lacking species have been highlighted in teal and light red, respectively. Putative cAIMs are highlighted in purple. Abbreviations: *H. s.*, *Homo sapiens*; *X. l., Xenopus laevis; D. m., Drosophila melanogaster; Ac. c., Acanthamoeba castellanii; N. g., Naegleria gruberi*; *D. p., Dictyostelium purpurea; V. v., Vitis vinifera; A. t., Arabidopsis thaliana* (trimmed sequence)*; C. s., Chlorella sorokiniana; C. r., Chlamydomonas reinhardtii; T. t., Tetrahymena thermophila; P. s. Phytopthora sojae; A. l., Albugo laibachii; A. c., Albugo candida; P. f., Piromyces finnis, N. c., Neocallimastix californiae; A. r., Anaeromyces robustus*. **(D, E) AcC53 and PfC53 do not have sAIM sequences and cannot interact with UFM1**. Ac: *Albugo candida*, Pf: *Piromyces finnis*. **(F, G) C53 IDR is essential for UFM1 interaction**. HsC53 (B) and AtC53 (C) IDRs are necessary to mediate the interaction with AtUFM1 and HsUFM1 respectively. MBP-AtC53$^{\Delta IDR}$: MBP-AtC53$^{(1\text{-}239,\ (KGSGSTSGSG)2,\ 373\text{-}549)}$; MBP-HsC53$^{\Delta IDR}$: HsC53$^{(1\text{-}262,\ (KGSGSTSGSG),\ 317\text{-}506)}$. **(H) AtC53^{sAIM} cannot interact with AtUFM1.** Individual or combinatorial mutations in sAIM1 (1A: W276A), sAIM2 (2A: W287A) and sAIM3 (3A: W335A) suggest sAIM1 is crucial for UFM1 interaction. (B, C, E, F, G) Bacterial lysates containing recombinant protein were mixed and pulled down with glutathione magnetic agarose beads. Input and bound proteins were visualized by immunoblotting with anti-GST and anti-MBP antibodies.

bioRxiv preprint doi: https://doi.org/10.1101/2022.04.26.489478; this version posted April 26, 2022. The copyright holder for this preprint (which was not certified by peer review) is the author/funder, who has granted bioRxiv a license to display the preprint in perpetuity. It is made available under aCC-BY 4.0 International license.

Fig. 3

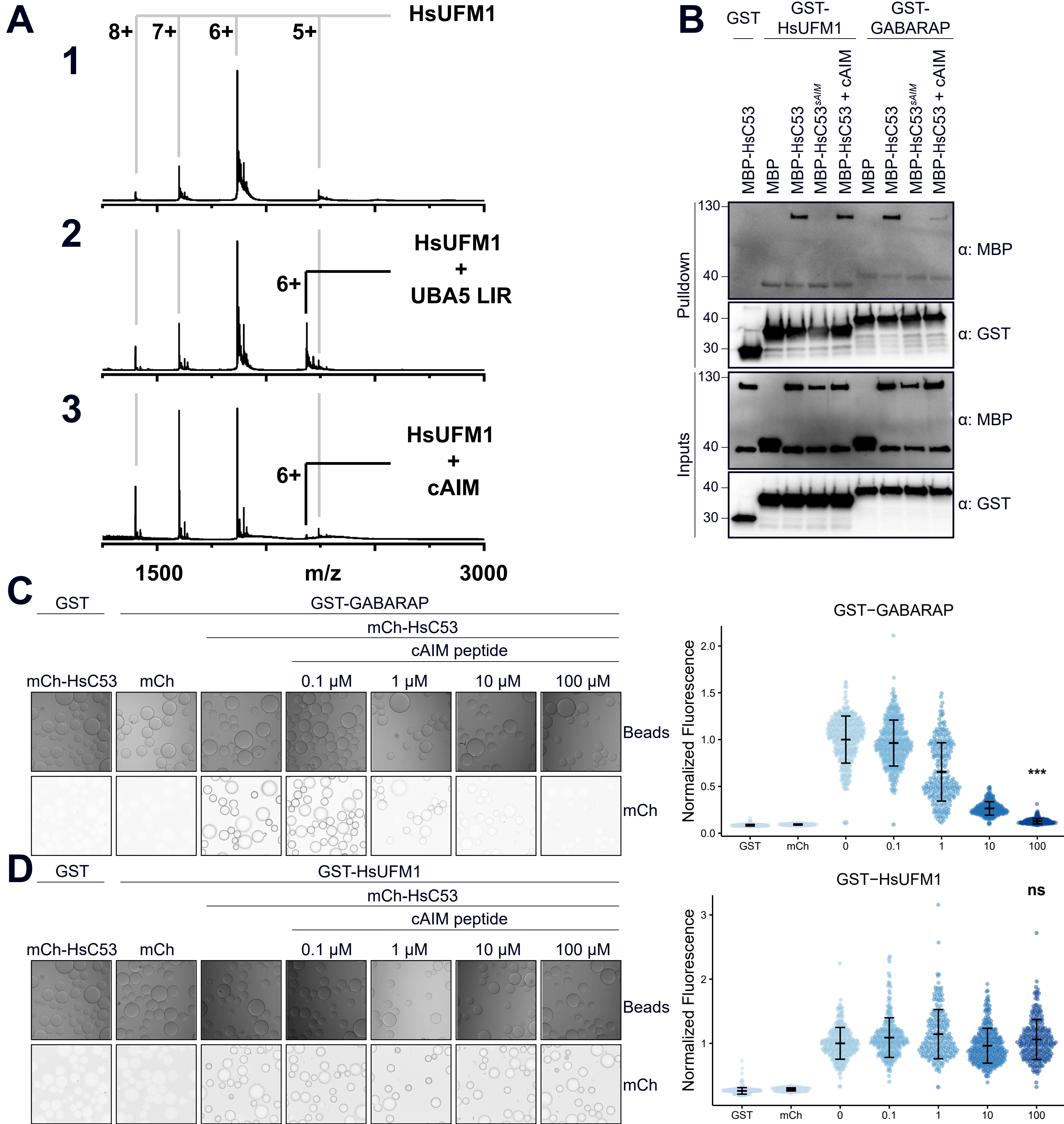

bioRxiv preprint doi: https://doi.org/10.1101/2022.04.26.489478; this version posted April 26, 2022. The copyright holder for this preprint (which was not certified by peer review) is the author/funder, who has granted bioRxiv a license to display the preprint in perpetuity. It is made available under aCC-BY 4.0 International license.

Figure 3. The canonical ATG8 Interacting Motif (cAIM) cannot outcompete C53-UFM1 interaction.

(A) Complex formation between cAIM peptide and UFM1. Native mass spectrometry (nMS) spectra of (1) HsUFM1 (5 µM), (2) HsUFM1 (5 µM) and UBA5 LIR peptide (25 µM) and (3) HsUFM1 (5 µM) and cAIM peptide (25 µM). UFM1 forms a 1:1 complex with the UBA5 LIR peptide. Only a negligible amount of 1:1 complex is formed between the cAIM peptide and UFM1, indicating a lower affinity interaction. **(B) The cAIM peptide cannot outcompete HsUFM1-HsC53 interaction.** Bacterial lysates containing recombinant protein were mixed and pulled down with glutathione magnetic agarose beads. Input and bound proteins were visualized by immunoblotting with anti-GST and anti-MBP antibodies. cAIM peptide was used to a final concentration of 200 µM. $HsC53^{sAIM}$: $HsC53^{W269A, W294A, W312A}$. **(C, D) Microscopy-based protein–protein interaction assays showing unlike GABARAP-C53 interaction, UFM1-C53 interaction is insensitive to cAIM peptide competition**. Glutathione-sepharose beads were prepared by incubating them with GST-GABARAP (C) or GST-HsUFM1 (D). The pre-assembled beads were then washed and mixed with 1 µM of HsC53 containing increasing concentrations of cAIM peptide (0-100 µM). The beads were then imaged using a confocal microscope. *Left Panel,* representative confocal images (inverted grayscale) for each condition are shown. *Right panel*, normalized fluorescence is shown for each condition with the mean (± SD) of 4 replicates. Unpaired two-samples Wilcoxon test with continuity correction was performed to analyze the differences between wild type and wild type with 100 µM AIM peptide. ns, not significant, p-value > 0.05, ***, p-value < 0.001. Total number of beads, mean, median, standard deviation and p-values are reported in Supplementary data 2.

bioRxiv preprint doi: https://doi.org/10.1101/2022.04.26.489478; this version posted April 26, 2022. The copyright holder for this preprint (which was not certified by peer review) is the author/funder, who has granted bioRxiv a license to display the preprint in perpetuity. It is made available under aCC-BY 4.0 International license.

Fig. 4

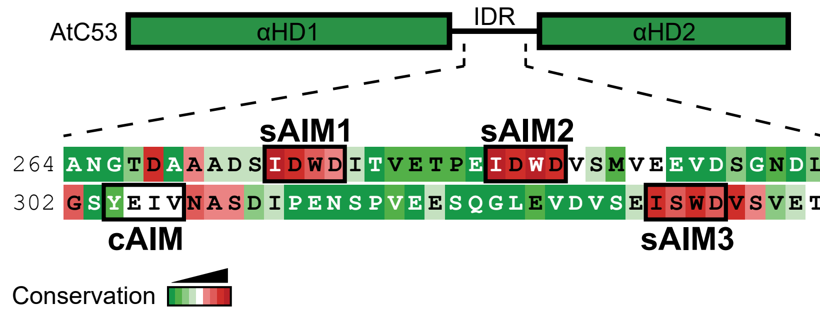

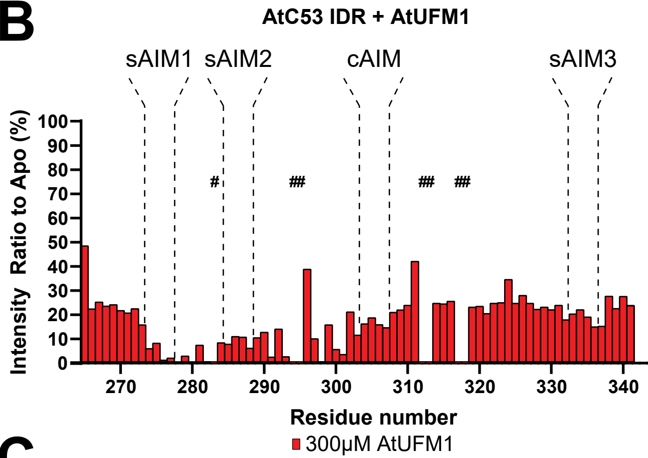

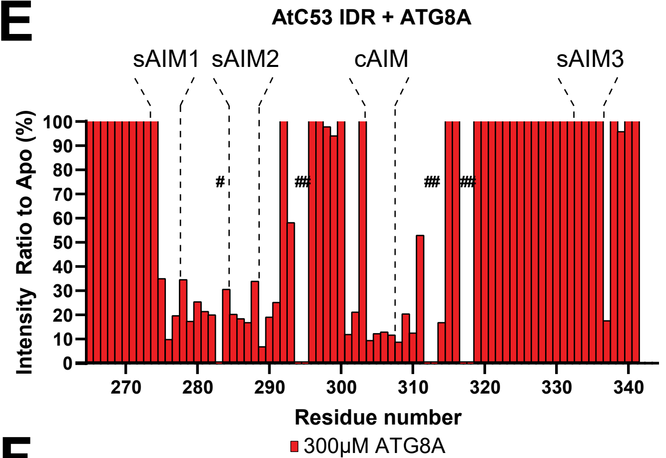

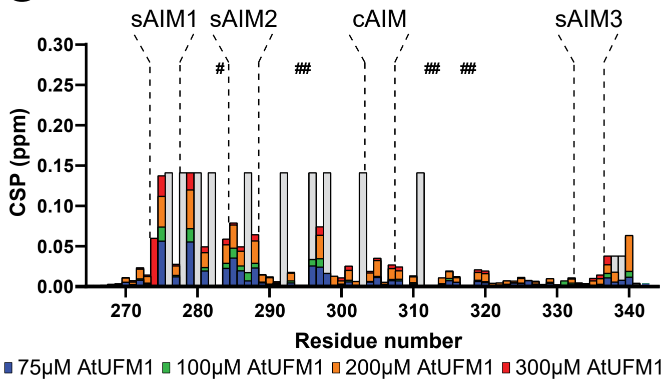

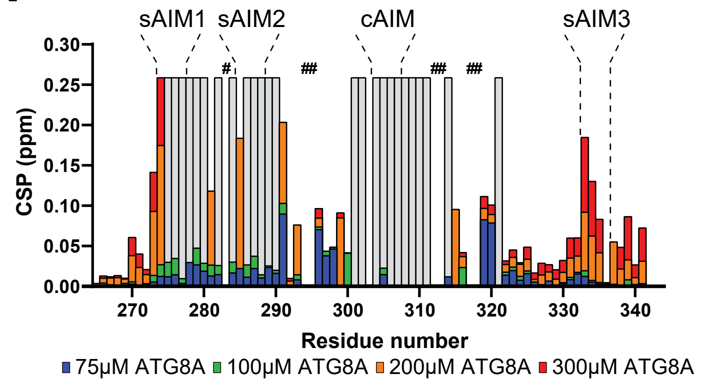

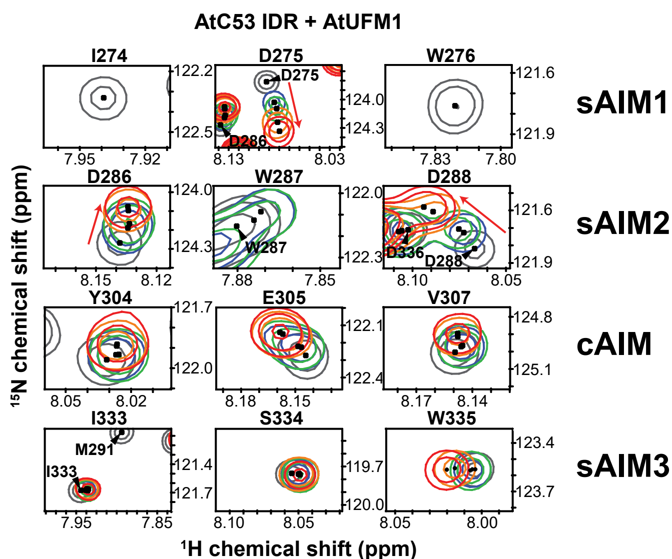

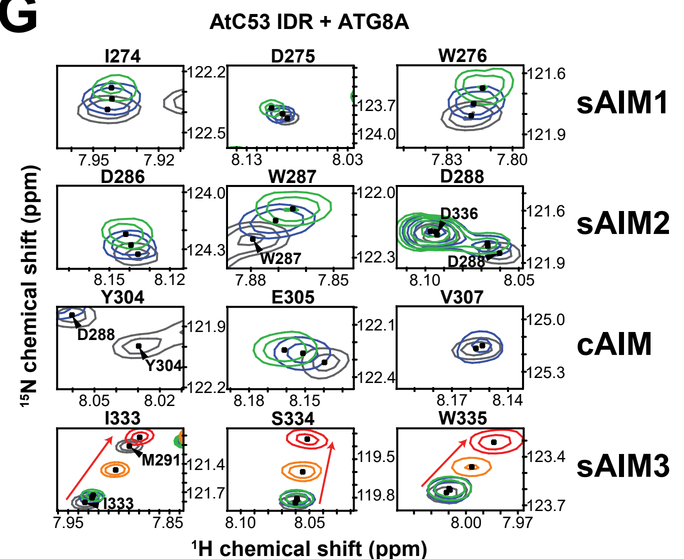

bioRxiv preprint doi: https://doi.org/10.1101/2022.04.26.489478; this version posted April 26, 2022. The copyright holder for this preprint (which was not certified by peer review) is the author/funder, who has granted bioRxiv a license to display the preprint in perpetuity. It is made available under aCC-BY 4.0 International license.

Figure 4. Comparative Nuclear Magnetic Resonance (NMR) spectroscopy analyses show C53 IDR-UFM1 interaction is different than C53 IDR-ATG8 interaction.

(A) AtC53 IDR harbours highly conserved canonical and shuffled ATG8 interaction motifs. Schematic representation of AtC53 domains with the primary sequence of C53 IDR. The AIM sequences and their conservation are indicated with rectangular boxes and a color code, respectively. **(B) Binding of AtUFM1 to AtC53 IDR leads to a general drop in signal intensity.** Intensity ratio broadening of AtC53 IDR (100 μM) in the presence of 300 μM AtUFM1. Bars corresponding to residues in the AIMs are highlighted. **(C) UFM1-IDR binding involves sAIM1 and sAIM2.** NMR chemical shift perturbations (CSP) of AtC53 IDR (100 μM) in the presence of 75 μM (blue), 100 μM (green), 200 μM (orange) and 300 μM (red) AtUFM1. **(D) AtC53 IDR spectra signals shift upon AtUFM1 addition in a concentration-dependent manner.** Insets of overlaid ^{1}H-^{15}N HSQC spectra of isotope-labeled AtC53 IDR (100 μM) showing chemical shift perturbations of individual peaks from backbone amides of AIM residues in their free (gray) or bound state to unlabeled AtUFM1. Chemical shifts are indicated with arrows. **(E) Binding of ATG8A AtC53 IDR leads to a localized signal intensity drop in sAIM1-2 and cAIM regions.** Intensity ratio broadening of C53 IDR (100 μM) in the presence of 300 μM ATG8A. Bars corresponding to residues in AIMs are highlighted. The intensity levels are capped at 100%. See Fig. S7E for the full plot. **(F) ATG8A-IDR binding involves sAIM1-2 and the cAIM regions.** NMR chemical shift perturbations (CSP) of AtC53 IDR (100 μM) in the presence of 75 μM (blue), 100 μM (green), 200 μM (orange) and 300 μM (red) ATG8A. **(G) AtC53 IDR spectra signals in the binding sites shift and broadened upon ATG8 addition.** Insets of overlaid ^{1}H-^{15}N HSQC spectra of isotope-labeled AtC53 IDR (100 μM) showing chemical shift perturbations of individual peaks from backbone amides of AIM residues in their free (gray) or bound state to unlabeled ATG8A. Unassigned AtC53 IDR residues are indicated by hashtags and HN resonances for residues that could not be assigned in the bound state are shown as gray bars (showing intensity signals of neighbor signals). Chemical shifts are indicated with arrows. Titrations with different concentrations of the ligands are colored similarly to C and F.

bioRxiv preprint doi: https://doi.org/10.1101/2022.04.26.489478; this version posted April 26, 2022. The copyright holder for this preprint (which was not certified by peer review) is the author/funder, who has granted bioRxiv a license to display the preprint in perpetuity. It is made available under aCC-BY 4.0 International license.

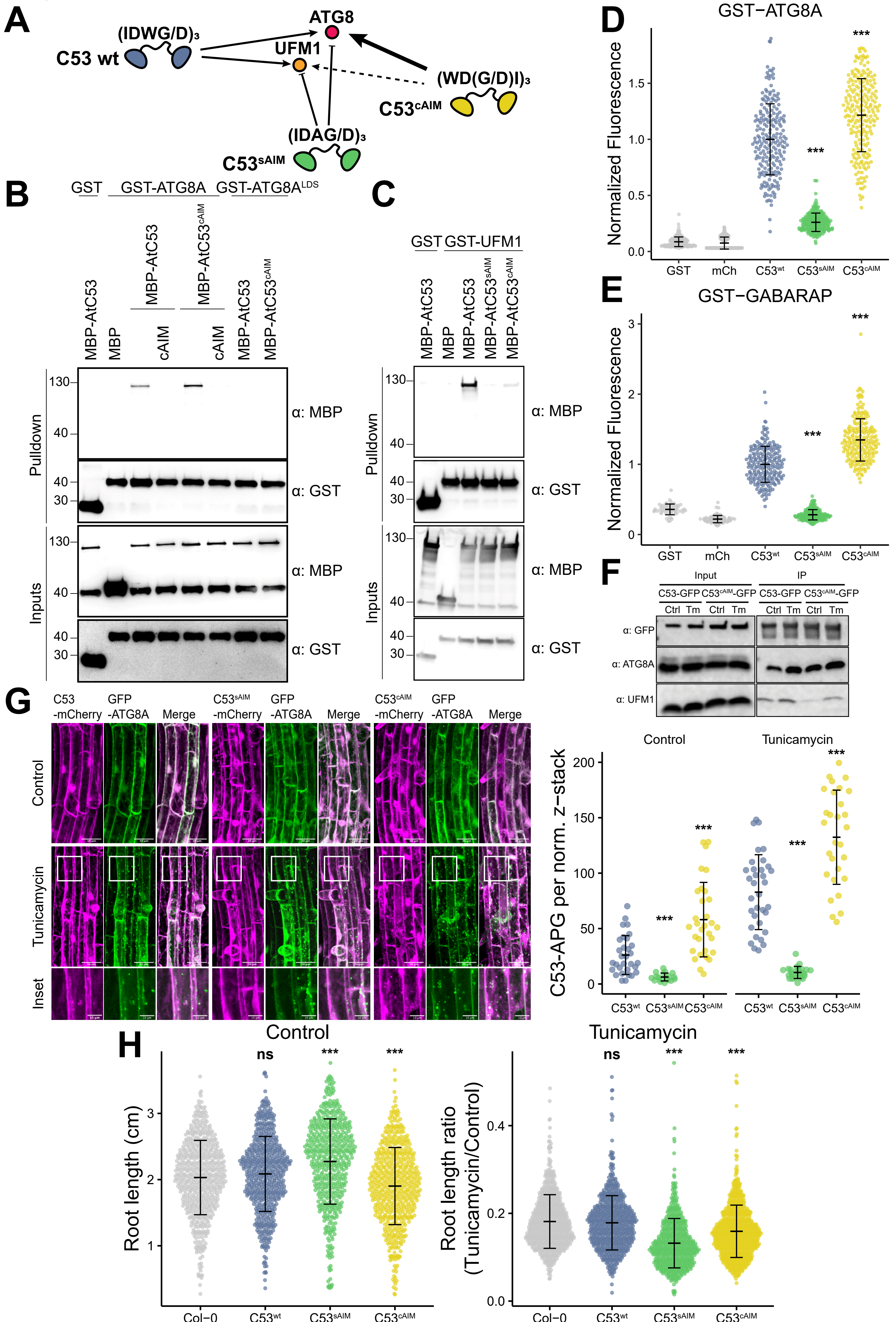

bioRxiv preprint doi: https://doi.org/10.1101/2022.04.26.489478; this version posted April 26, 2022. The copyright holder for this preprint (which was not certified by peer review) is the author/funder, who has granted bioRxiv a license to display the preprint in perpetuity. It is made available under aCC-BY 4.0 International license.

Figure 5. C53 sAIM sequences are essential for ER stress tolerance.

(A) Diagram summarizing our hypothesis that conversion of sAIMs to cAIMs would prevent C53-UFM1 interaction and strengthen C53-ATG8 interaction. (B, C) Conversion of sAIM into cAIM leads to reduced UFM1 binding and stronger ATG8 interaction. Bacterial lysates containing recombinant proteins were mixed and pulled down with glutathione magnetic agarose beads. Input and bound proteins were visualized by immunoblotting with anti-GST and anti-MBP antibodies. AtC53^{sAIM}: AtC53 $^{(W276A,\ W287A,\ W335A)}$; AtC53^{cAIM}: AtC53$^{(IDWD274WDDI,\ IDWD285WDDI,\ IDWD333WDDI)}$; ATG8^{LDS}: ATG8^{YL50AA}. **(D, E) Microscopy-based protein–protein interaction assays showing C53^{cAIM} has increased affinity towards ATG8 or GABARAP.** Glutathione-sepharose beads were prepared by incubating them with GST-ATG8A (D) or GST-GABARAP (E). The pre-assembled beads were then washed and mixed with (D) 1 μM of HsC53, 1 μM of HsC53^{sAIM} or 1 μM of HsC53^{cAIM} mutants or (E) 1 μM of AtC53, 1 μM of AtC53^{sAIM} or 1 μM of AtC53^{cAIM} mutants. HsC53^{sAIM}: HsC53$^{(W269A,\ W294A,\ W312A)}$; HsC53^{cAIM}: HsC53$^{(IDWG267WDGI,\ IDWG292WDGI,\ IDWG310WDGI)}$. The beads were then imaged using a confocal microscope. Representative confocal images for each condition are shown in figure S10A, B. Normalized fluorescence is shown for each condition with the mean (± SD) of 3 replicate. Unpaired two-samples Wilcoxon test with continuity correction was performed to analyze the differences between wild type and mutants. ***, p-value < 0.001. Total number of beads, mean, median, standard deviation and p-values are reported in Supplementary data 2. **(F) *In vivo* pull downs showing sAIM to cAIM conversion strengthens C53-ATG8 association and weakens C53-UFM1 association.** 6-day old *Arabidopsis* seedlings expressing AtC53-GFP, AtC53^{cAIM}-GFP in *c53* mutant background were incubated in liquid 1/2 MS medium with 1% sucrose supplemented with DMSO as control (Ctrl) or 10 μg/ml tunicamycin (Tm) for 16 hours and used for co-immunoprecipitation. Lysates were incubated with GFP-Trap Magnetic Agarose, input and bound proteins were detected by immunoblotting using the respective antibodies as indicated. **(G) AtC53^{cAIM} forms more GFP-ATG8A colocalizing puncta upon ER stress.** *Upper Panel*, representative confocal images of transgenic *Arabidopsis* seedlings co-expressing C53-mCherry (magenta), C53^{sAIM}-mCherry and C53^{cAIM}-mCherry with GFP-ATG8a in *c53* mutant background under normal condition and after tunicamycin stress. 6-day old seedlings were incubated in liquid 1/2 MS medium with 1% sucrose supplemented with DMSO as control or tunicamycin (10 μg/ml) for 6 hours before imaging. Scale bars, 30 μm. Inset scale bars, 10 μm. *Right Panel*, Quantification of the C53-autophagosomes (C53-APG) per normalized Z-stacks. Bars represent the mean (± SD) of at least twenty roots from 3 biological replicates for each genotype and treatment. Unpaired two-samples Wilcoxon test with continuity correction was performed to analyze the differences between wild type and mutants. ***, p-value < 0.001. **(H) AtC53^{cAIM} mutant is sensitive to ER stress.** Root length quantification of 7-day old *Arabidopsis* seedlings grown vertically on sucrose-free 1/2 MS agar plates supplemented with DMSO control (*Left Panel*, absolute root length in centimeters (cm)) or 100 ng/ml tunicamycin (*Right Panel*, ratio between the root length of tunicamycin treated seedlings and the average of respective control condition). T4 transgenic lines expressing C53-GFP, C53^{sAIM}-GFP and C53^{cAIM}-GFP in *c53* mutant background were used. Statistical results of more than 500 seedlings from 3 biological repeats per each genotype for control and tunicamycin treated condition are shown. Bars represent the mean (± SD) of 3 biological replicates. Unpaired two-samples Wilcoxon test with continuity correction was performed to analyze the differences between wild type and mutants. ns, p-value > 0.05, ***, p-value < 0.001.

bioRxiv preprint doi: https://doi.org/10.1101/2022.04.26.489478; this version posted April 26, 2022. The copyright holder for this preprint (which was not certified by peer review) is the author/funder, who has granted bioRxiv a license to display the preprint in perpetuity. It is made available under aCC-BY 4.0 International license.

Fig. S1

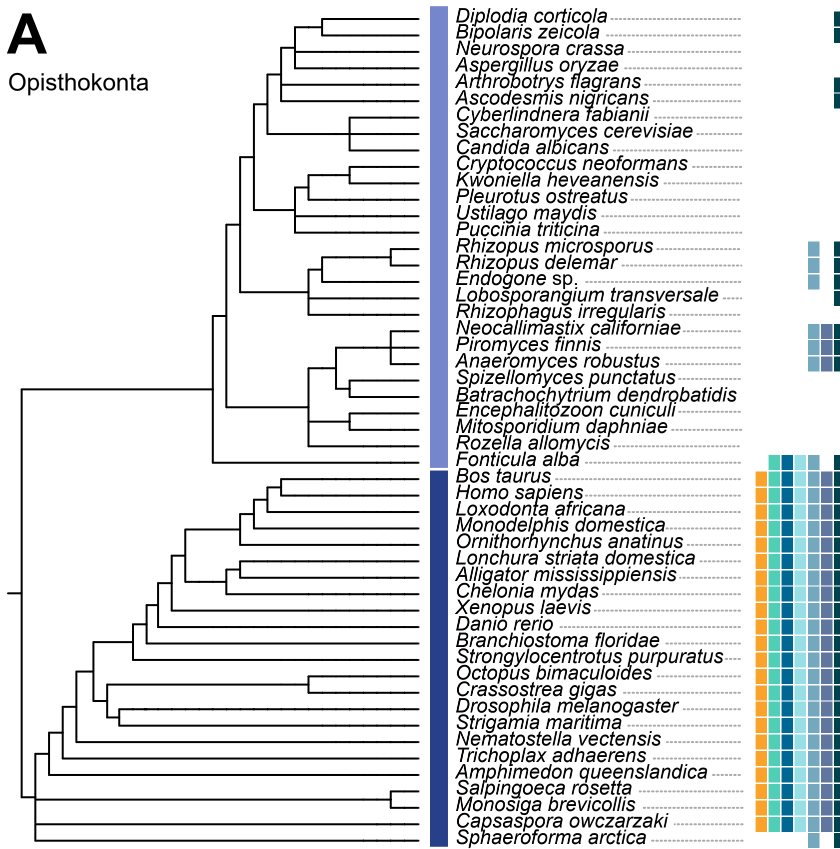

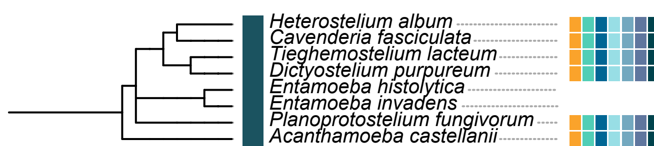

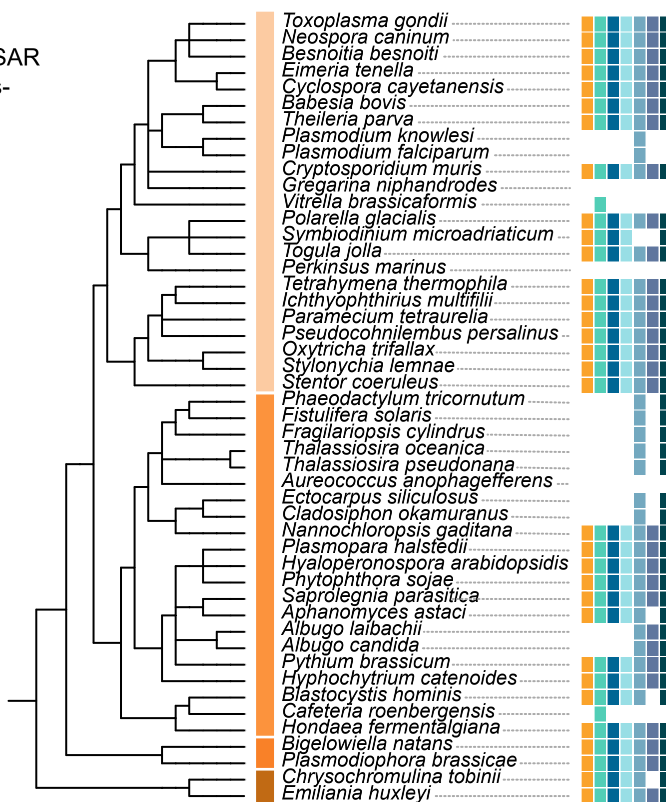

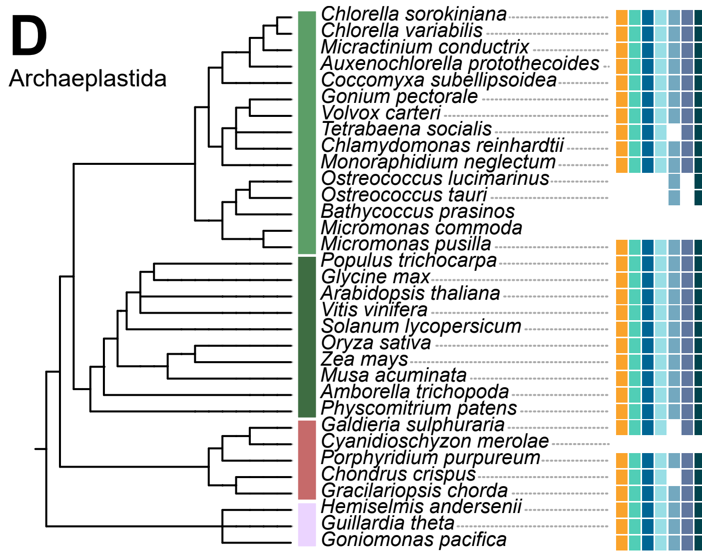

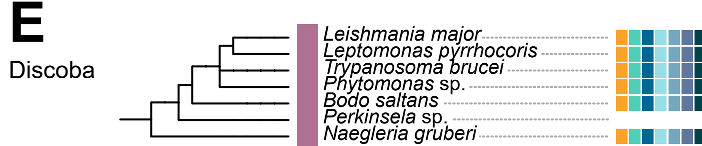

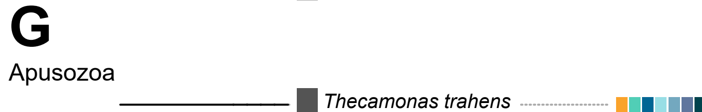

Proteins
- UFM1
- UFSP2
- UFC1
- UBA5
- DDRGK1
- C53
- UFL1

Eukaryotic group
- Holomycota (e.g., Fungi)
- Holozoa (e.g., Animals)
- Amoebozoans
- Alveolates
- Stramenopiles
- Rhizarians
- Haptophytes
- Green algae
- Plants
- Red algae
- Cryptomonads
- Discoba
- Metamonada
- Apusozoa

bioRxiv preprint doi: https://doi.org/10.1101/2022.04.26.489478; this version posted April 26, 2022. The copyright holder for this preprint (which was not certified by peer review) is the author/funder, who has granted bioRxiv a license to display the preprint in perpetuity. It is made available under aCC-BY 4.0 International license.

Figure S1. An expanded version of the tree depicted in Figure 1A, displaying the presence and absence of UFMylation proteins across the eukaryotic taxa. The tree has been divided into eukaryotic supergroups including the Opisthokonta (**A**), Amoebozoa (**B**), Haptophyta and SAR (**C**), Archaeplastida (**D**), Discoba (**E**), Metamonada (**F**), and Apusozoa (**G**).

bioRxiv preprint doi: https://doi.org/10.1101/2022.04.26.489478; this version posted April 26, 2022. The copyright holder for this preprint (which was not certified by peer review) is the author/funder, who has granted bioRxiv a license to display the preprint in perpetuity. It is made available under aCC-BY 4.0 International license.

Fig. S2

A

Trimmed RPL26 alignment

119 ... 147

UFM1 present

```
Homo sapiens                    ERKAKSRQVGKEKG-KYKEETIEKMQE--
Xenopus laevis                  ERKAKSRQVGKEKG-KYKEETIEKMQE--
Drosophila melanogaster         ERRGKGRLLGKDKG-KYTEETAAQPMETA
Naegleria gruberi               KRKAEARSTQANKG-KFTEETVKQ-----
Dictyostelium purpureum         ERKNRSSE---EKG-KITKEQV--TAEVN
Arabidopsis thaliana RPL26A     ERKAKGRAADKEKGTKFTSEDV--MQNVD
Arabidopsis thaliana RPL26B     ERKANGRAADKEKGTKFSAEDV--MENVD
Vitis vinifera                  DRKAKGRAADKDKGTKFTAEDI--MQSVD
Chlamydomonas reinhardtii       ERKKVARAAEKGKG-KFTEQDV-AMTNVD
Chlorella sorokiniana           ERKRAGKG--ADKG-KFTEAEVAAMENVD
Tetrahymena thermophila         TRKAASLK---TKG-KHTVA---------
Toxoplasma gondii               ERKSRATT----KG-KYTEKDV-AMSQVD
Phytophthora sojae              ERKNRAVS-ETEKG-KFTEQDV-AMANVD
```

UFM1 absent

```
Albugo laibachii                ERKNRAVG-DKNKS-KYTEADV-AMASVD
Albugo candida                  ERKNRAVG-DKNKS-KYTEADV-TMASVD
Cyanidioschyzon merolae         KRKERASL---MNA-RVTPSRSAVMADVD
Ectocarpus siliculosus          ARKDRSRNGGKPAA-GAADADV-NMAGVD
Thalassiosira oceanica          DRKNRNKK-----G-NDV-----EMTNVD
Fragilariopsis cylindrus        EAKAANNN----KE-KSSDA---PMSNVD
Ustilago maydis                 ARKSGSKK---EAA-ETKDN---------
Saccharomyces cerevisiae        QRKGGKLE---------------------
Diplodia corticola              ERIGKGRE--AAKA-KTTKA---------
Rhizophagus irregularis         DRKNRVLKKDENKA-LKKDEDKAKIEEMD
Piromyces finnis                ERKAANKQ---------------------
Neocallimastix californiae      ERKAANKQ-----G-KPA-----------
Anaeromyces robustus            ERKAANKQ-------------------LE
Plasmodium falciparum           DRKAAKEN---------------------
Trichomonas vaginalis           ERRRAGREILAKLG-HNKK----------
Sphaeroforma arctica            ERKNRDTK---------------------
Entamoeba histolytica           AKKAESRKSYKELV-AKRNEEVAKMSKPT
```

B

RPL26 tail

• RPL26 tail lysines

TwinCons Score

6
4
2
0

0 50 100 150

Trimmed alignment position

bioRxiv preprint doi: https://doi.org/10.1101/2022.04.26.489478; this version posted April 26, 2022. The copyright holder for this preprint (which was not certified by peer review) is the author/funder, who has granted bioRxiv a license to display the preprint in perpetuity. It is made available under aCC-BY 4.0 International license.

Figure S2. Conservation analysis of RPL26 shows that the ufmylated tail region is divergent.

(A) Multiple sequence alignment of RPL26 showing the conservation of the C-terminal tail in species with and without UFM1. Lysine residues that are ufmylated have been highlighted. (**B) TwinCons analysis comparing the sequence conservation of RPL26.** The tail region is highly polymorphic.

bioRxiv preprint doi: https://doi.org/10.1101/2022.04.26.489478; this version posted April 26, 2022. The copyright holder for this preprint (which was not certified by peer review) is the author/funder, who has granted bioRxiv a license to display the preprint in perpetuity. It is made available under aCC-BY 4.0 International license.

Fig. S3

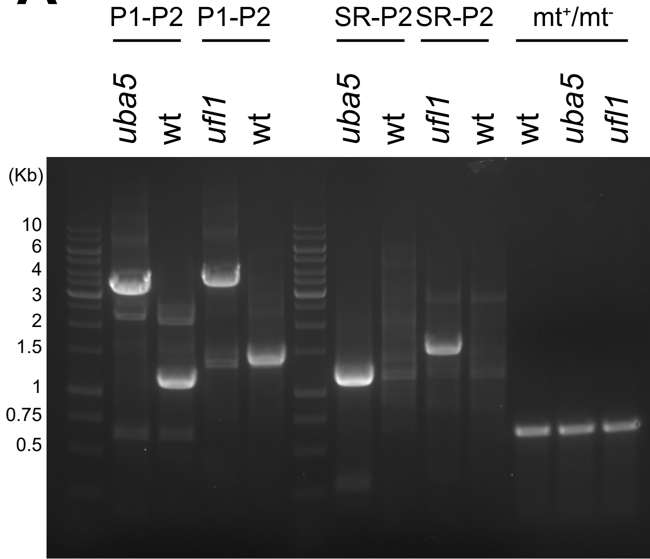

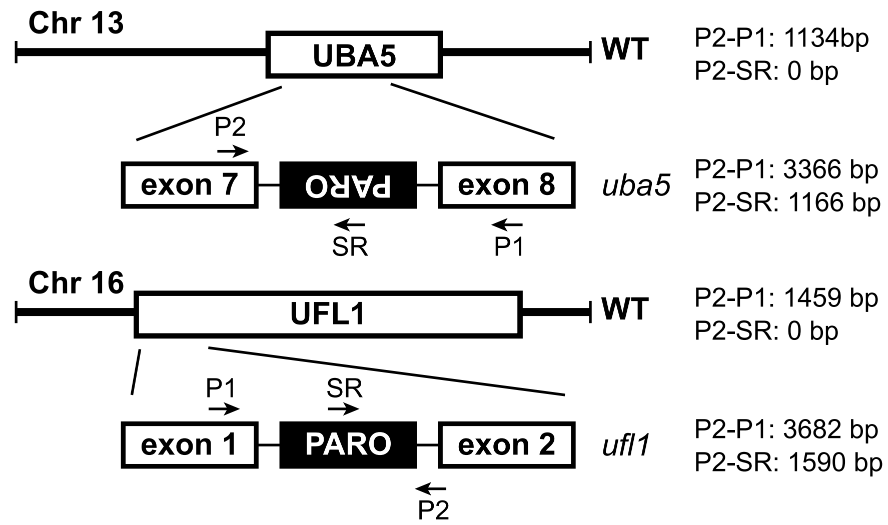

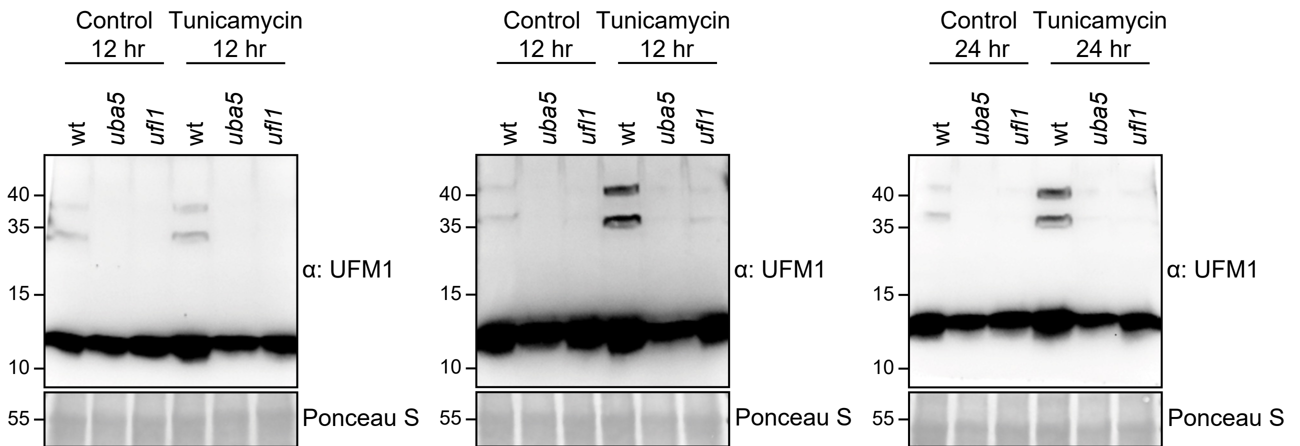

bioRxiv preprint doi: https://doi.org/10.1101/2022.04.26.489478; this version posted April 26, 2022. The copyright holder for this preprint (which was not certified by peer review) is the author/funder, who has granted bioRxiv a license to display the preprint in perpetuity. It is made available under aCC-BY 4.0 International license.

Figure S3. Characterization of the *Chlamydomonas reinhardtii* UFMylation pathway mutants.

(A) Genotyping of *C. reinhardtii uba5* and *ufl1* mutants. *Left Panel*, mating type (mt +/-) and insertion site PCR products from purified genomic DNA samples prepared from wt, *uba5* and *ufl1* genotypes. PCR products were run on a 1% (w/v) agarose gel. DNA size markers are reported in Kb. **(B) Schematic diagram indicating the insertion site of the mutagenic cassette (PARO) in *ufl1* and *uba5* mutants.** Primers are indicated with arrows and expected PCR products from wild type and mutants are reported next to each respective diagram. **(C) RPL26 mono- and di-UFMylation is lost in *uba5* and *ufl1* mutants**. Cells were either left untreated or treated for 24 hours with 200 ng/mL tunicamycin. Protein extracts were analyzed by immunoblotting with anti-UFM1 antibodies. Total proteins were analyzed by Ponceau S staining. Quantification is shown in Figure 1C.

bioRxiv preprint doi: https://doi.org/10.1101/2022.04.26.489478; this version posted April 26, 2022. The copyright holder for this preprint (which was not certified by peer review) is the author/funder, who has granted bioRxiv a license to display the preprint in perpetuity. It is made available under aCC-BY 4.0 International license.

Fig. S4

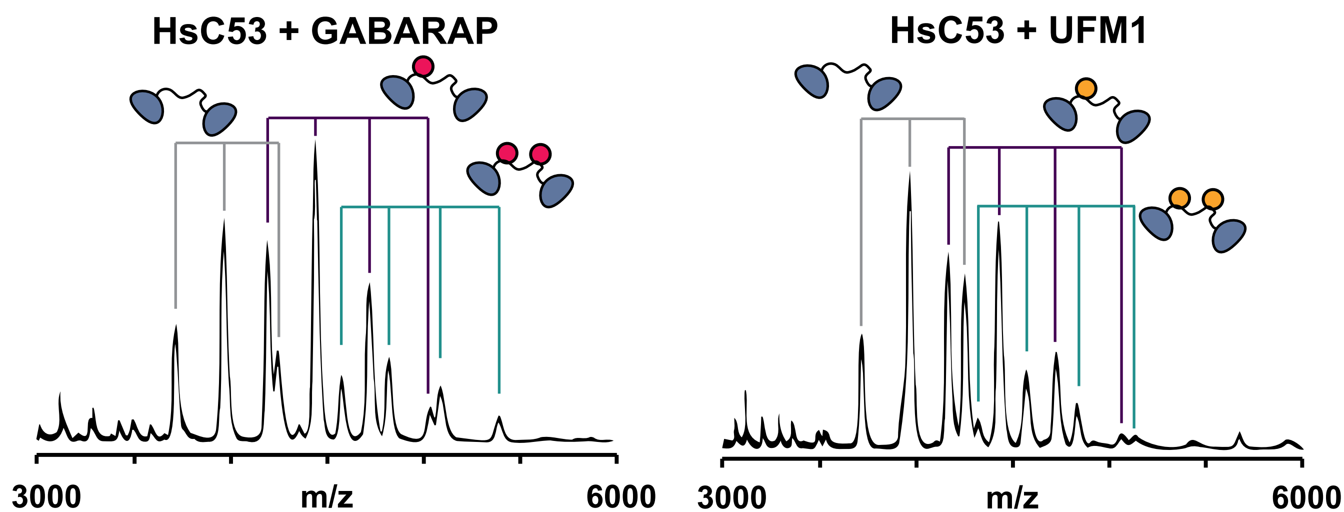

bioRxiv preprint doi: https://doi.org/10.1101/2022.04.26.489478; this version posted April 26, 2022. The copyright holder for this preprint (which was not certified by peer review) is the author/funder, who has granted bioRxiv a license to display the preprint in perpetuity. It is made available under aCC-BY 4.0 International license.

Figure S4. Native Mass-Spectrometry (nMS) spectra of HsC53 with GABARAP or HsUFM1 show very similar binding profiles. *Upper Panel*, GABARAP (4 μM) and HsC53 (2 μM). *Right Panel*, HsUFM1 (4 μM) and HsC53 (2 μM). Binding of HsC53 to GABARAP and HsUFM1 is observed in 1:1 (violet) and 1:2 ratios (teal)**.**

bioRxiv preprint doi: https://doi.org/10.1101/2022.04.26.489478; this version posted April 26, 2022. The copyright holder for this preprint (which was not certified by peer review) is the author/funder, who has granted bioRxiv a license to display the preprint in perpetuity. It is made available under aCC-BY 4.0 International license.

Fig. S5

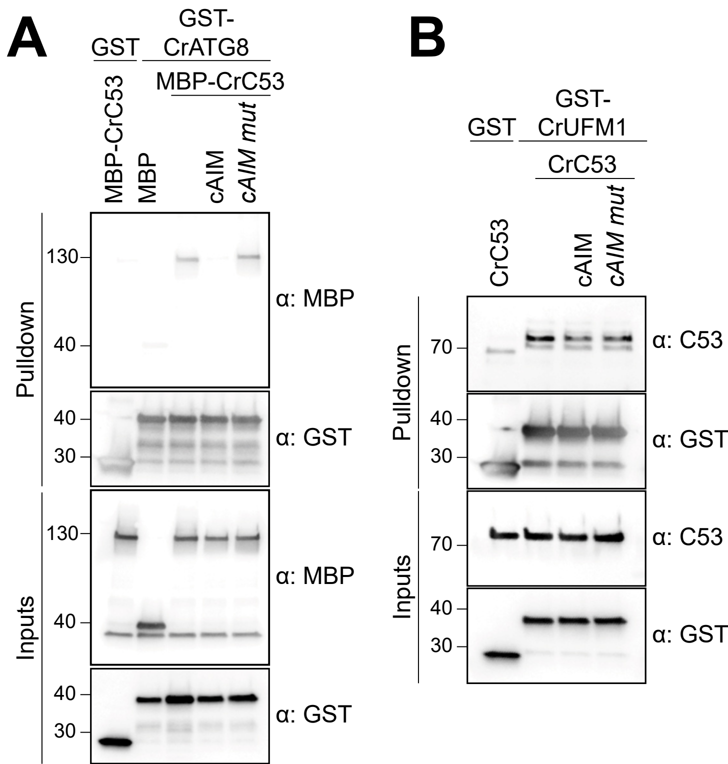

bioRxiv preprint doi: https://doi.org/10.1101/2022.04.26.489478; this version posted April 26, 2022. The copyright holder for this preprint (which was not certified by peer review) is the author/funder, who has granted bioRxiv a license to display the preprint in perpetuity. It is made available under aCC-BY 4.0 International license.

Figure S5. The canonical ATG8 Interacting Motif (cAIM) peptide cannot outcompete C53-UFM1 interaction for *C. reinhardtii* (Cr).

(A) CrC53 binds CrATG8A in a cAIM-dependent manner. (B) CrC53 binds UFM1 in a cAIM-independent manner. Bacterial lysates containing recombinant protein or purified recombinant proteins were mixed and pulled down with glutathione magnetic agarose beads. Input and bound proteins were visualized by immunoblotting with anti-GST, anti-MBP or anti-AtC53 antibodies. cAIM wild type or mutant peptides were used to a final concentration of 200 μM.

bioRxiv preprint doi: https://doi.org/10.1101/2022.04.26.489478; this version posted April 26, 2022. The copyright holder for this preprint (which was not certified by peer review) is the author/funder, who has granted bioRxiv a license to display the preprint in perpetuity. It is made available under aCC-BY 4.0 International license.

Fig. S6

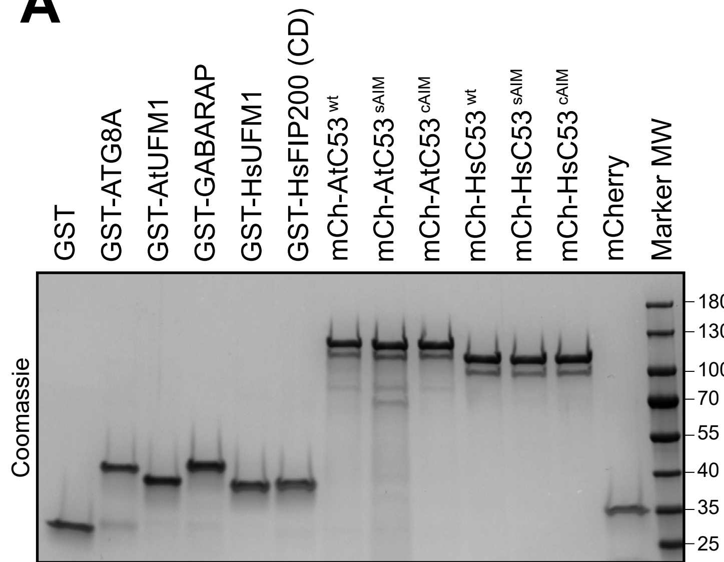

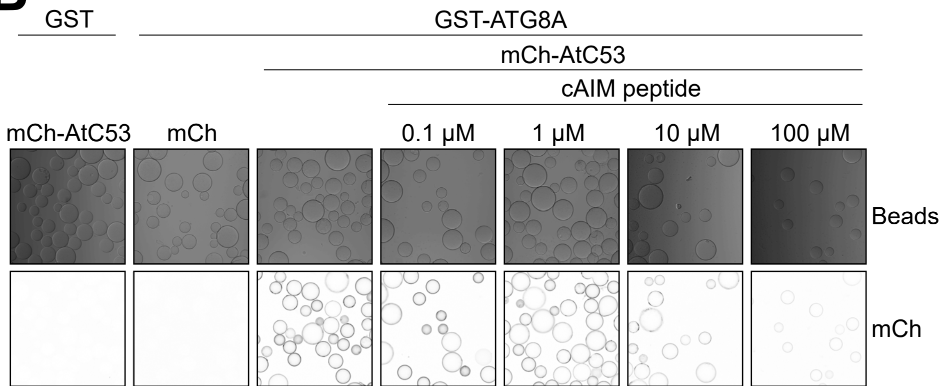

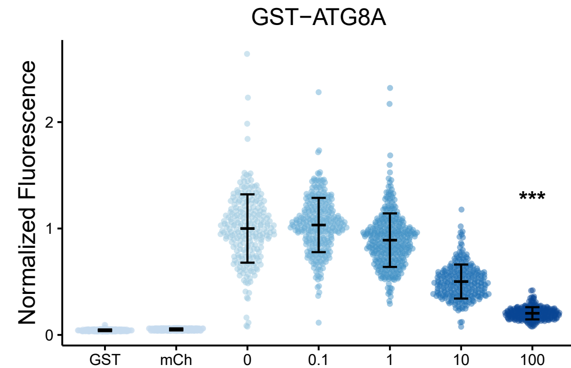

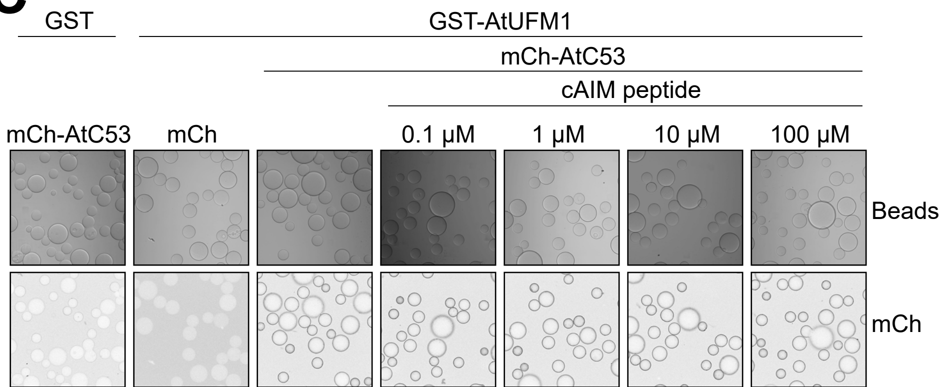

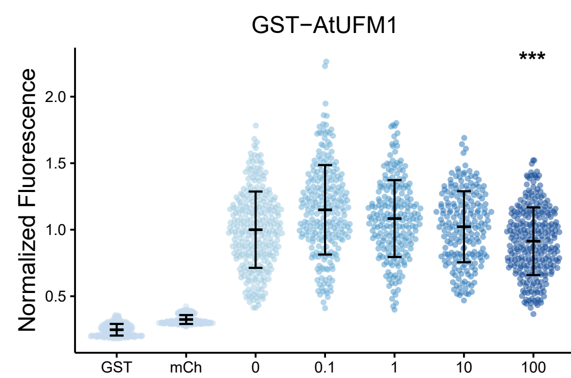

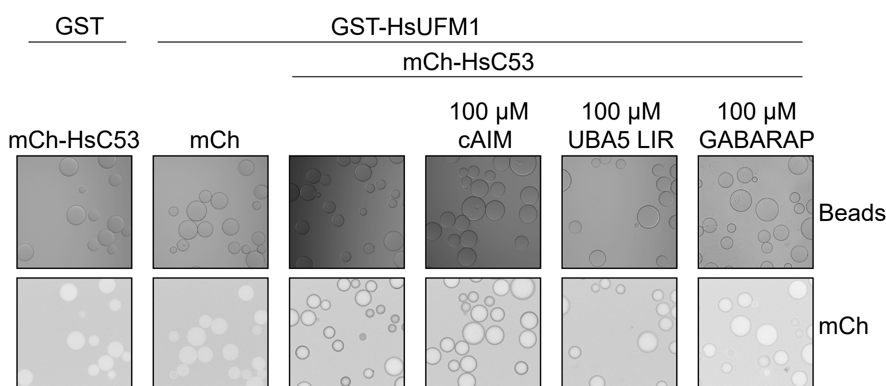

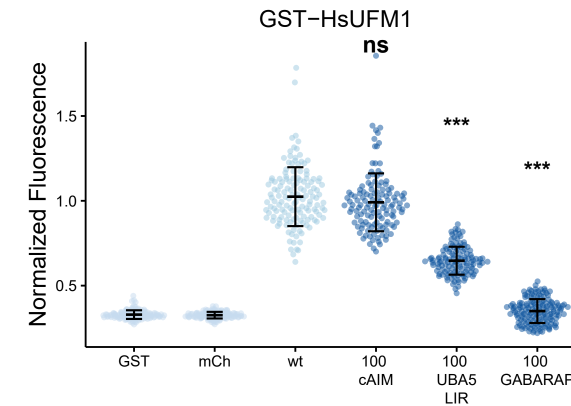

bioRxiv preprint doi: https://doi.org/10.1101/2022.04.26.489478; this version posted April 26, 2022. The copyright holder for this preprint (which was not certified by peer review) is the author/funder, who has granted bioRxiv a license to display the preprint in perpetuity. It is made available under aCC-BY 4.0 International license.

Figure S6. The canonical ATG8 Interacting Motif (cAIM) cannot outcompete C53-UFM1 interaction.

(A) Purified proteins used for the protein-protein interaction microscopy binding assays. Recombinant proteins were analyzed for purity by SDS-PAGE followed by Coomassie staining. Marker molecular weights (MW) are indicated in kDa. mCh: mCherry. **(B, C) Microscopy-based protein–protein interaction assays showing unlike ATG8A-C53 interaction, UFM1-C53 interaction is insensitive to cAIM peptide competition**. Glutathione-sepharose beads were prepared by incubating them with GST-ATG8A (C) or GST-AtUFM1 (D). The pre-assembled beads were then washed and mixed with 1 µM of AtC53 containing increasing concentrations of cAIM peptide (0-100 µM). The beads were then imaged using a confocal microscope. *Left Panel,* representative confocal images (inverted grayscale) for each condition are shown. *Right panel*, normalized fluorescence is shown for each condition with the mean (± SD) of 2 independent replicates containing 2 technical replicates. Unpaired two-samples Wilcoxon test with continuity correction was performed to analyze the differences between wild type without cAIM peptide and wild type with 100 µM cAIM peptide. *, p-value < 0.05, ***, p-value < 0.001. Total number of beads, mean, median, standard deviation and p-values are reported in Supplementary data 2. **(D) Microscopy-based protein–protein interaction assays showing UBA5 LIR peptide and GABARAP can compete for C53 interaction with UFM1**. Glutathione-sepharose beads were prepared by incubating them with GST-HsUFM1. The pre-assembled beads were then washed and mixed with 1 µM of HsC53 with either 100 µM cAIM peptide, 100 µM UBA5 LIR peptide or 100 µM GABARAP. The beads were then imaged using a confocal microscope. *Left Panel,* representative confocal images (inverted grayscale) for each condition are shown. *Right panel*, normalized fluorescence is shown for each condition with the mean (± SD). Unpaired two-samples Wilcoxon test with continuity correction was performed to analyze the differences between wild type and wild type mixed with either cAIM peptide, UBA5 LIR peptide or GABARAP. ns, p-value > 0.05, ***, p-value < 0.001. Total number of beads, mean, median, standard deviation and p-values are reported in Supplementary data 2.

bioRxiv preprint doi: https://doi.org/10.1101/2022.04.26.489478; this version posted April 26, 2022. The copyright holder for this preprint (which was not certified by peer review) is the author/funder, who has granted bioRxiv a license to display the preprint in perpetuity. It is made available under aCC-BY 4.0 International license.

Fig. S7

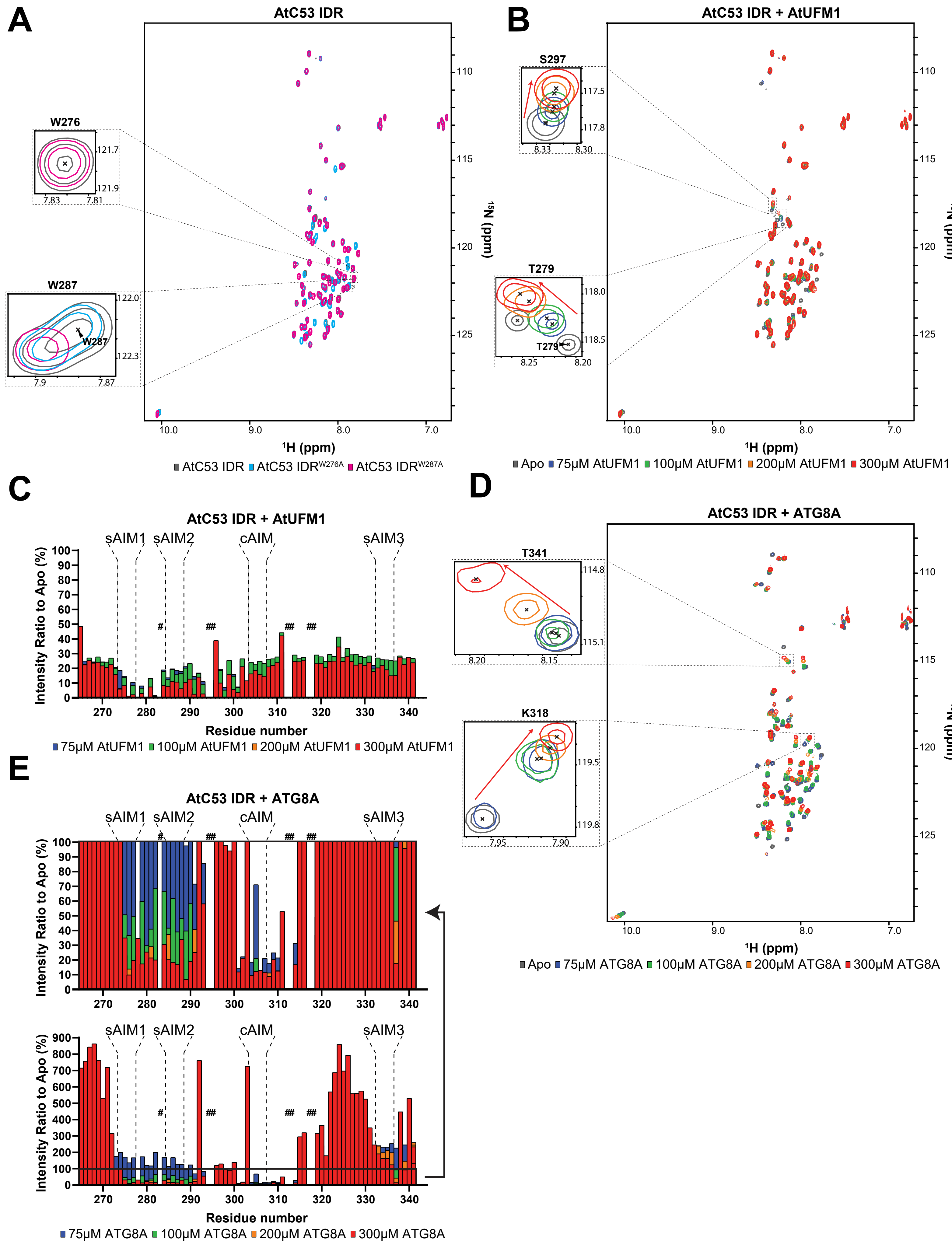

bioRxiv preprint doi: https://doi.org/10.1101/2022.04.26.489478; this version posted April 26, 2022. The copyright holder for this preprint (which was not certified by peer review) is the author/funder, who has granted bioRxiv a license to display the preprint in perpetuity. It is made available under aCC-BY 4.0 International license.

Figure S7. Structural characterization of AtC53 IDR binding to AtUFM1 and ATG8A using NMR spectroscopy.

(A) Validation of AtC53 IDR backbone resonance assignments. Overlaid ^{1}H-^{15}N HSQC spectra of isotope-labeled AtC53 IDR (grey), AtC53 IDR^{W276A} (cyan) and AtC53 IDR^{W287A} (magenta). Insets of resonances corresponding to residues W276 and W287 are shown. **(B) Addition of AtUFM1 changes the magnetic resonance of specific residues in AtC53.** Overlaid ^{1}H-^{15}N HSQC spectra of isotope-labeled AtC53 IDR in their free (gray) or bound state to 75 μM (blue), 100 μM (green), 200 μM (orange) and 300 μM (red) unlabeled AtUFM1. Examples of individual peaks that shift upon binding are shown as insets. Chemical shifts are indicated with arrows. **(C) Signal intensity changes in AtC53 IDR upon binding of AtUFM1 are concentration dependent.** Intensity ratio broadening of AtC53 IDR (100 μM) in the presence of 75 μM (blue), 100 μM (green), 200 μM (orange) and 300 μM (red) AtUFM1. Bars corresponding to residues in AIMs are highlighted. Unassigned AtC53 IDR residues are indicated by hashtags. **(D) Addition of ATG8A affects a greater number of residues in the AtC53 IDR spectra.** Overlaid ^{1}H-^{15}N HSQC spectra of isotope-labeled AtC53 IDR in their free (gray) or bound state to 75 μM (blue), 100 μM (green), 200 μM (orange) and 300 μM (red) unlabeled ATG8A. Insets of individual peaks that shifted upon binding are shown. Chemical shifts are indicated with arrows. **(E) Signal intensity changes in AtC53 IDR upon binding of ATG8A are concentration dependent.** Intensity ratio broadening of AtC53 IDR (100 μM) in the presence of 75 μM (blue), 100 μM (green), 200 μM (orange) and 300 μM (red) ATG8A. Top panel represents an inset of lower panel. Unassigned AtC53 IDR residues are indicated by hashtags. Bars corresponding to residues in AIMs are highlighted.

bioRxiv preprint doi: https://doi.org/10.1101/2022.04.26.489478; this version posted April 26, 2022. The copyright holder for this preprint (which was not certified by peer review) is the author/funder, who has granted bioRxiv a license to display the preprint in perpetuity. It is made available under aCC-BY 4.0 International license.

Fig. S8

A

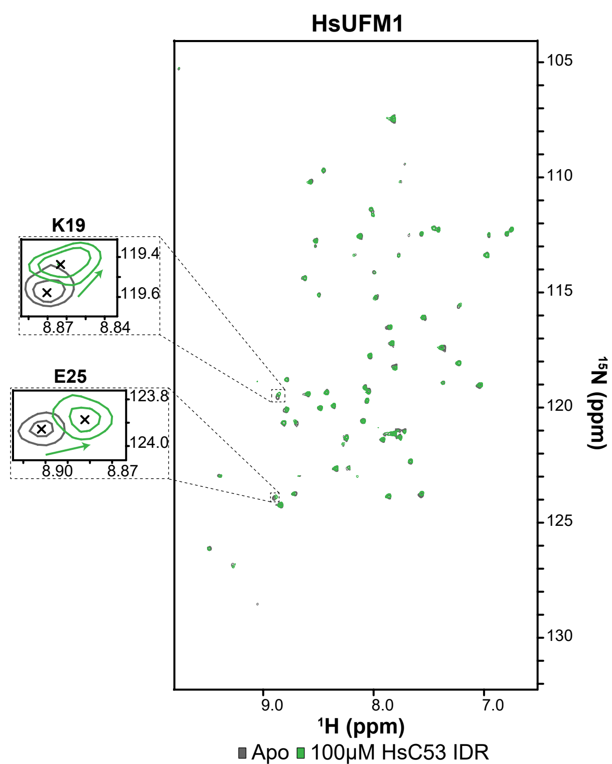

B

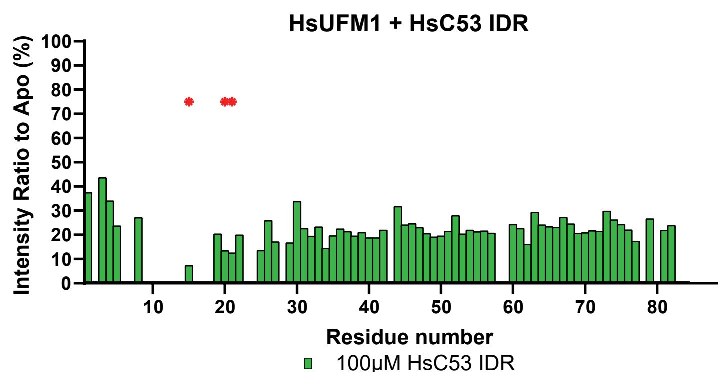

C

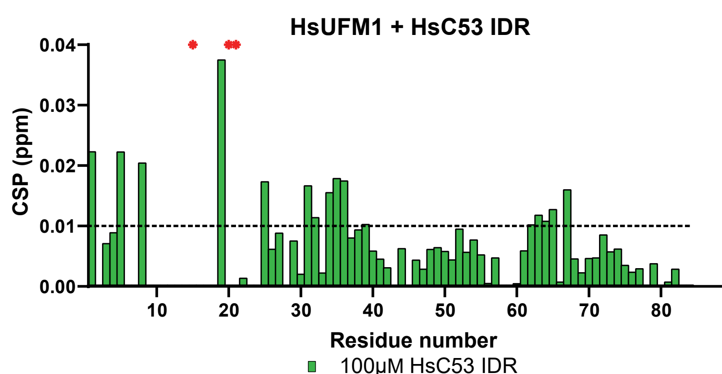

D

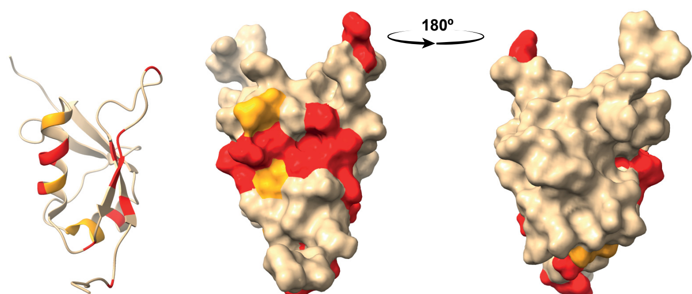

E

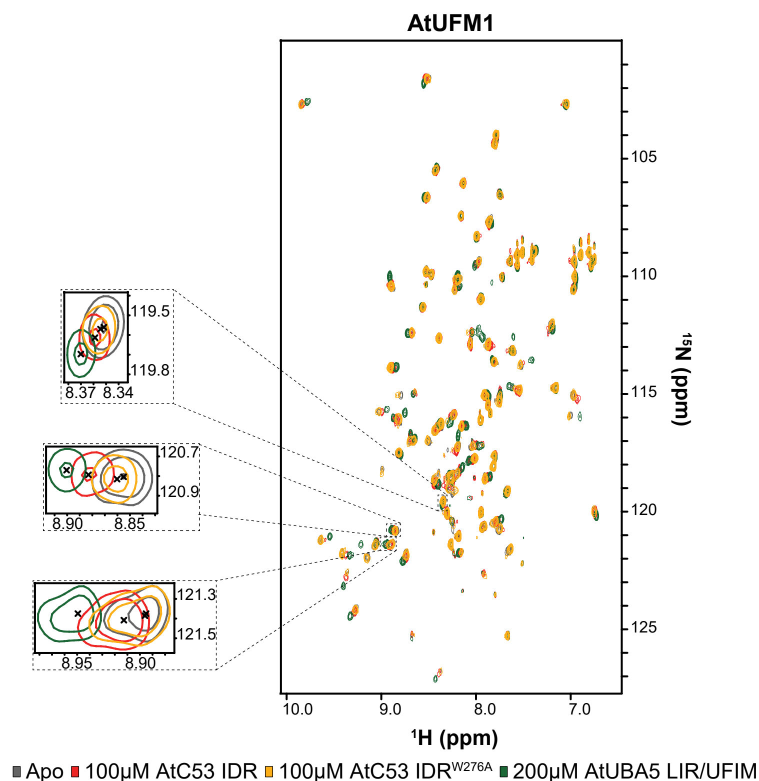

bioRxiv preprint doi: https://doi.org/10.1101/2022.04.26.489478; this version posted April 26, 2022. The copyright holder for this preprint (which was not certified by peer review) is the author/funder, who has granted bioRxiv a license to display the preprint in perpetuity. It is made available under aCC-BY 4.0 International license.

Figure S8. Structural characterization of UFM1 binding to C53 IDR using NMR spectroscopy.

(A) A small number of residues are affected by the addition of HsC53 IDR as shown in the HsUFM1 spectra. Overlaid ^{1}H-^{15}N HSQC spectra of isotope-labeled HsUFM1 in their free (gray) or bound state to 100 µM unlabeled HsC53 IDR (green). Insets of individual peaks that shift upon binding are shown. **(B) HsC53 IDR binding to HsUFM1 causes general signal intensity drop in HsUFM1 spectra.** Intensity ratio broadening of HsUFM1 (100 µM) in the presence of 100 µM HsC53 IDR (green). HN resonances for residues that could not be assigned in the bound state are shown as red asterisks. **(C) Chemical shift perturbations (CSPs) in the HsUFM1 spectrum (grey) upon addition of 100 µM HsC53 IDR (green).** HN resonances for residues that could not be assigned in the bound state are shown as red asterisks. The dashed line represents S.D. **(D) Three-dimensional mapping of residues showing CSP in HsUFM1 NMR spectra upon HsC53 IDR binding.** CSPs were mapped on the UFM1 structure (PDB: 1WXS) presented schematically on the left plot and as a surface representation in two projections on the right plot. Residues that are not affected or are slightly (CSP < 0.01), intermediately (0.01 < CSP < 0.015), or strongly (CSP > 0.015) affected by the binding are colored in tan, orange and red, respectively. **(E) AtC53 IDR binding to AtUFM1 is similar to that of AtUBA5 and involves sAIM1.** Overlaid ^{1}H-^{15}N HSQC spectra of isotope-labeled AtUFM1 in their free (gray) or bound state to 100 µM unlabeled AtC53 IDR (red), 100 µM unlabeled AtC53 IDR^{W276A} (yellow) or AtUBA5 LIR/UFIM (green). Insets of chemical shift perturbations of individual peaks are shown.

bioRxiv preprint doi: https://doi.org/10.1101/2022.04.26.489478; this version posted April 26, 2022. The copyright holder for this preprint (which was not certified by peer review) is the author/funder, who has granted bioRxiv a license to display the preprint in perpetuity. It is made available under aCC-BY 4.0 International license.

Fig. S9

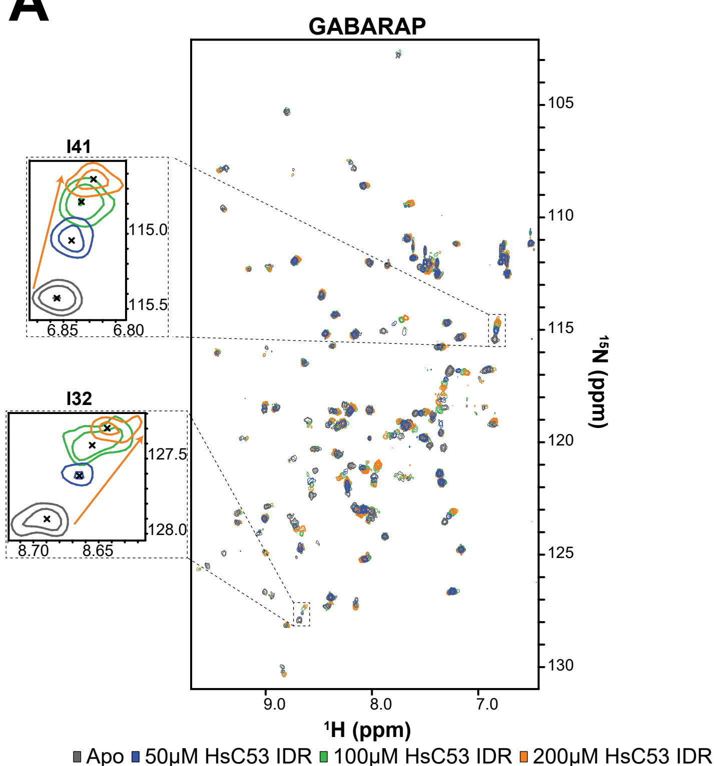

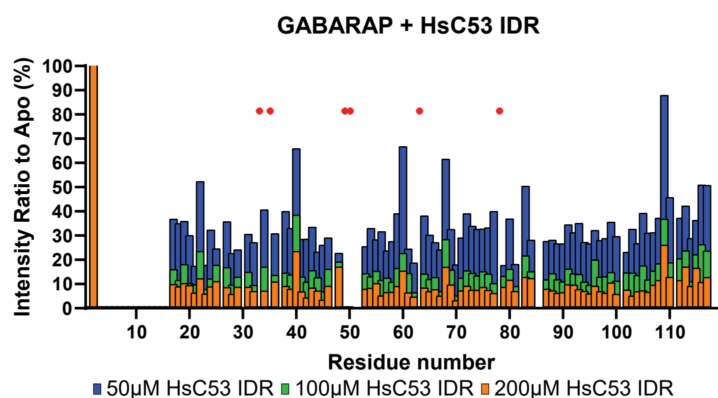

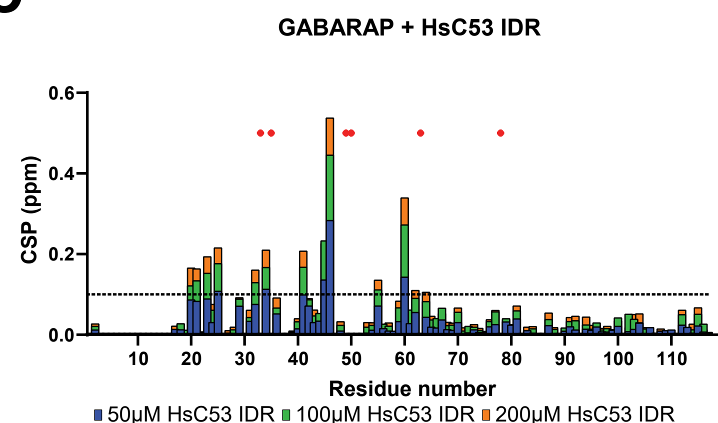

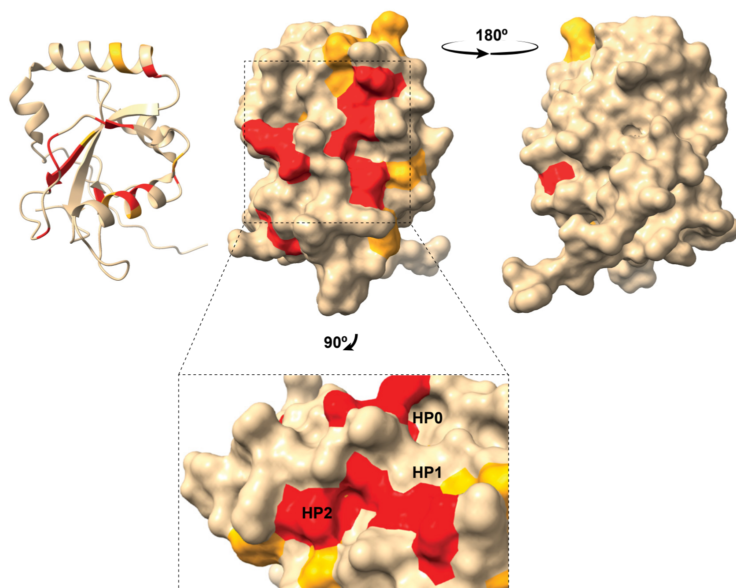

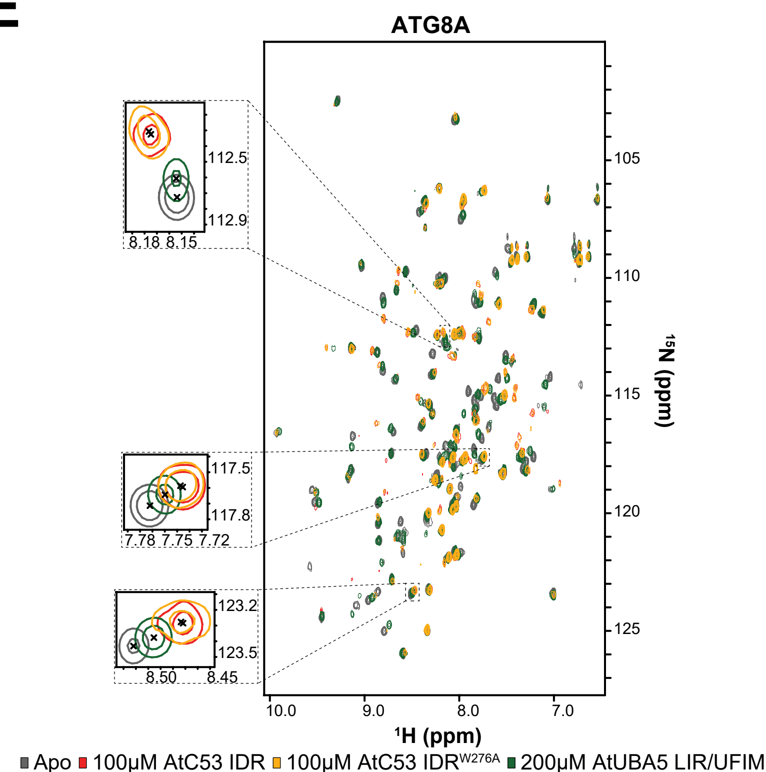

bioRxiv preprint doi: https://doi.org/10.1101/2022.04.26.489478; this version posted April 26, 2022. The copyright holder for this preprint (which was not certified by peer review) is the author/funder, who has granted bioRxiv a license to display the preprint in perpetuity. It is made available under aCC-BY 4.0 International license.

Figure S9. Structural characterization of ATG8 binding to C53 IDR using NMR spectroscopy.

(A) Addition of HsC53 IDR affects numerous residues in the GABARAP spectra. Overlaid ^{1}H-^{15}N HSQC spectra of isotope-labeled GABARAP in their free (gray) or bound state to 50 µM (blue), 100 µM (green) or 200 µM (orange) unlabeled HsC53 IDR. Insets of individual peaks that shifted upon binding are shown. **(B) HsC53 IDR binding to GABARAP causes a general signal intensity drop in GABARAP spectra.** Intensity ratio broadening of GABARAP (100µM) in the presence of 50 µM (blue), 100 µM (green) or 200 µM (orange) unlabeled HsC53 IDR. HN resonances for residues that could not be assigned in the bound state are shown as red asterisks. **(C) NMR chemical shift perturbations (CSP) of GABARAP in the presence of 50 µM (blue), 100 µM (green) or 200 µM (orange) HsC53 IDR.** HN resonances for residues that could not be assigned in the bound state are shown as red asterisks. The dashed line represents S.D. **(D) Three-dimensional mapping of residues showing CSP in GABARAP NMR spectra upon HsC53 IDR binding.** CSPs were mapped on the GABARAP structure (PDB: 6HB9) presented schematically on the left plot and as a surface representation in two projections on the right plot. Residues that are not affected or are slightly (CSP < 0.1), intermediately (0.1 < CSP < 0.2), or strongly (CSP > 0.2) affected by the binding are colored in tan, orange and red, respectively. The inset highlights the position of the HP0, HP1 and HP2 hydrophobic pockets in GABARAP. **(E) AtC53 IDR binding to ATG8 is similar to that of AtUBA5.** Overlaid ^{1}H-^{15}N HSQC spectra of isotope-labeled ATG8A in their free (gray) or bound state to 100 µM unlabeled AtC53 IDR (red), 100 µM unlabeled AtC53 IDR^{W276A} (yellow) or 200 µM AtUBA5 LIR/UFIM (green). Insets of chemical shift perturbations of individual peaks are shown.

bioRxiv preprint doi: https://doi.org/10.1101/2022.04.26.489478; this version posted April 26, 2022. The copyright holder for this preprint (which was not certified by peer review) is the author/funder, who has granted bioRxiv a license to display the preprint in perpetuity. It is made available under aCC-BY 4.0 International license.

Fig. S10

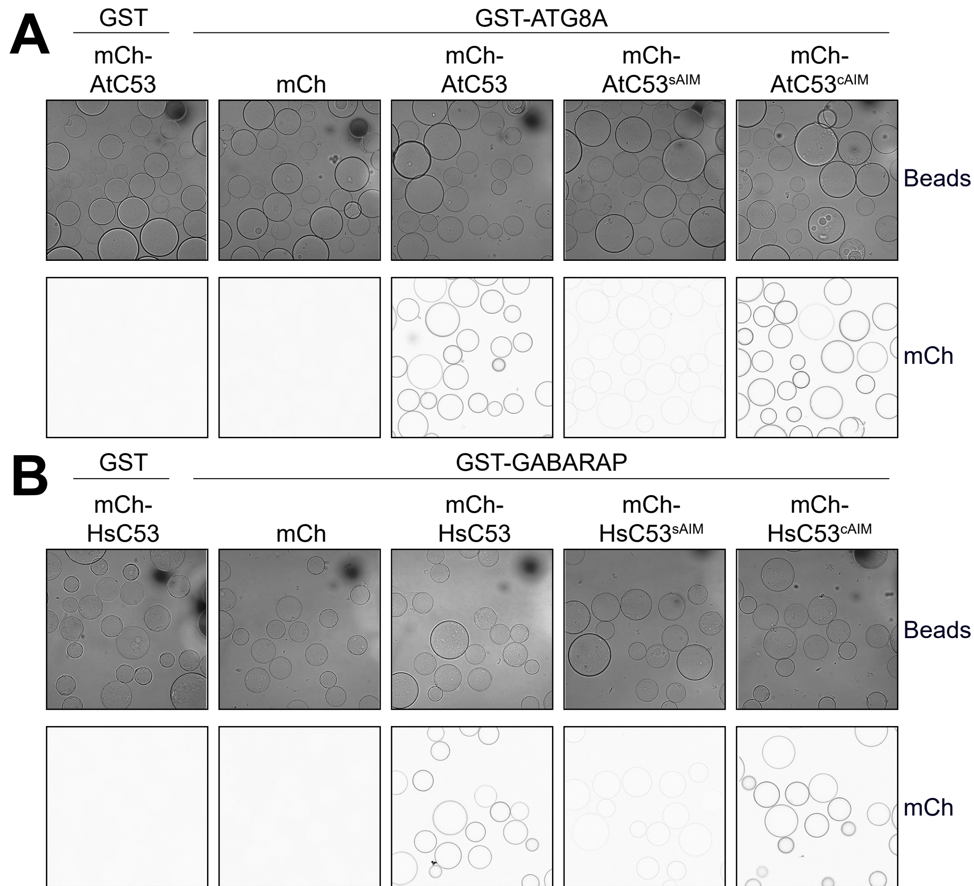

bioRxiv preprint doi: https://doi.org/10.1101/2022.04.26.489478; this version posted April 26, 2022. The copyright holder for this preprint (which was not certified by peer review) is the author/funder, who has granted bioRxiv a license to display the preprint in perpetuity. It is made available under aCC-BY 4.0 International license.

Figure S10. Microscopy-based protein–protein interaction assays showing C53^{cAIM} has increased affinity towards ATG8 or GABARAP.

(A, B) Representative confocal images (inverted grayscale) for each condition from Figure 5 D, E are shown.

bioRxiv preprint doi: https://doi.org/10.1101/2022.04.26.489478; this version posted April 26, 2022. The copyright holder for this preprint (which was not certified by peer review) is the author/funder, who has granted bioRxiv a license to display the preprint in perpetuity. It is made available under aCC-BY 4.0 International license.

Fig. S11

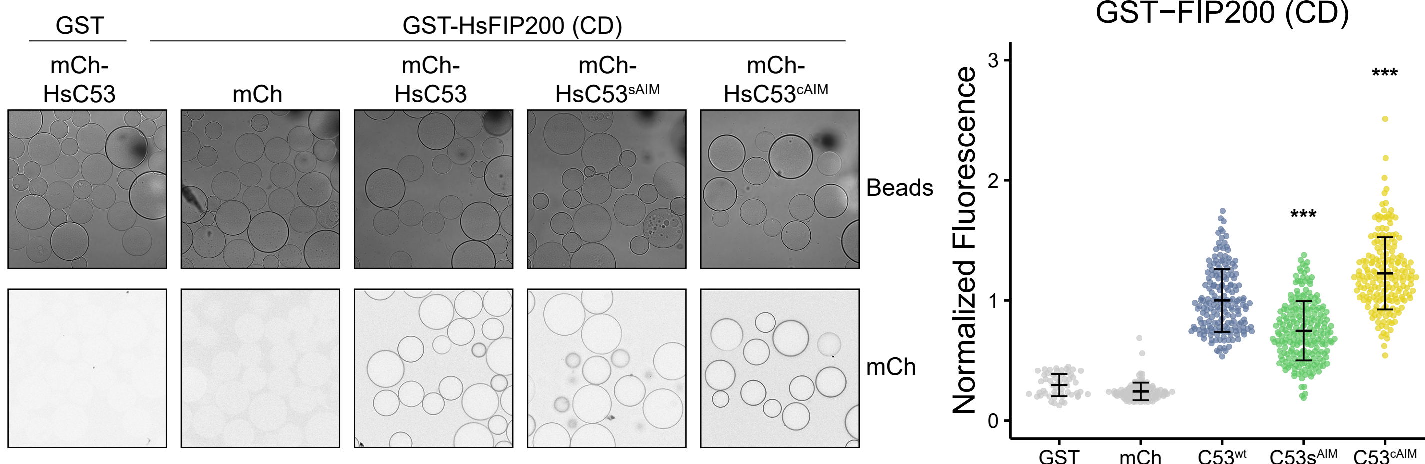

bioRxiv preprint doi: https://doi.org/10.1101/2022.04.26.489478; this version posted April 26, 2022. The copyright holder for this preprint (which was not certified by peer review) is the author/funder, who has granted bioRxiv a license to display the preprint in perpetuity. It is made available under aCC-BY 4.0 International license.

Fig. S11. C53-HsFIP200 Claw domain (CD) interaction is also mediated by the sAIM sequences and strengthened by sAIM to cAIM conversion. Glutathione-sepharose beads were prepared by incubating them with GST-FIP200 CD. The pre-assembled beads were then washed and mixed with 1 μM of HsC53, 1 μM of $HsC53^{sAIM}$ or 1 μM of $HsC53^{cAIM}$ mutants. The beads were then imaged using a confocal microscope. *Left Panel,* representative confocal images (inverted grayscale) for each condition are shown. *Right panel*, normalized fluorescence is shown for each condition with the mean (± SD) of 2 independent replicates containing 2 technical replicates. Unpaired two-samples Wilcoxon test with continuity correction was performed to analyze the differences between wild type and mutants. ***, p-value < 0.001. Total number of beads, mean, median, standard deviation and p-values are reported in Supplementary data 2.

bioRxiv preprint doi: https://doi.org/10.1101/2022.04.26.489478; this version posted April 26, 2022. The copyright holder for this preprint (which was not certified by peer review) is the author/funder, who has granted bioRxiv a license to display the preprint in perpetuity. It is made available under aCC-BY 4.0 International license.

Fig. S12

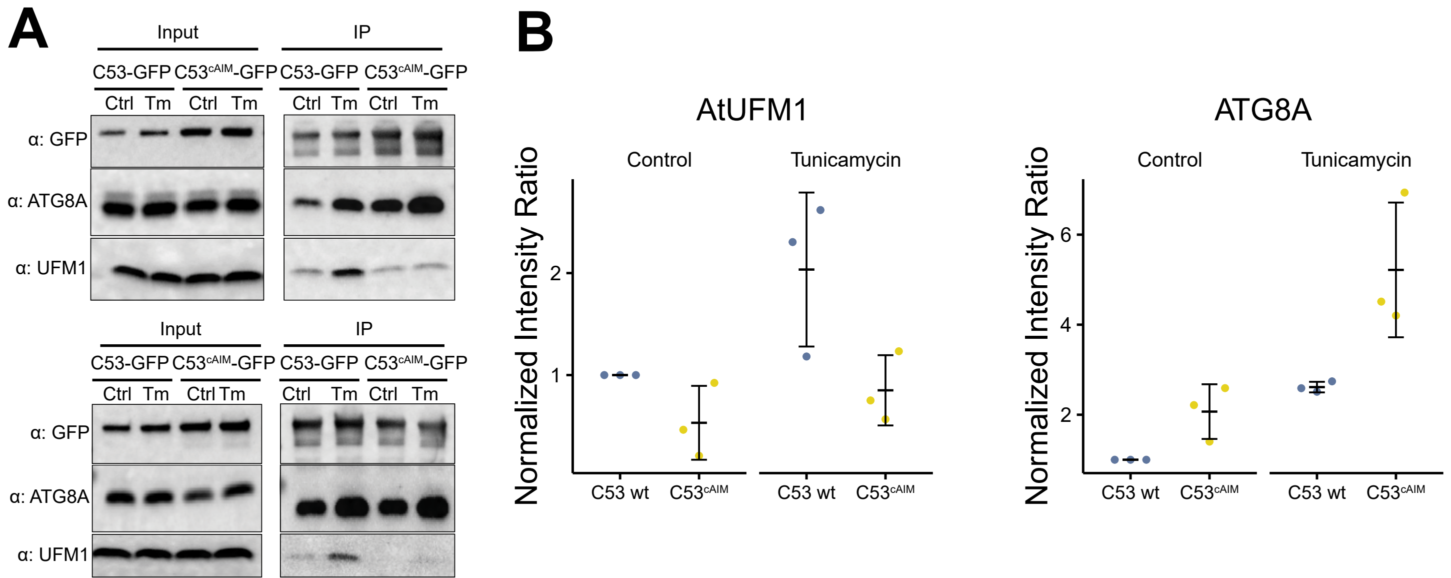

bioRxiv preprint doi: https://doi.org/10.1101/2022.04.26.489478; this version posted April 26, 2022. The copyright holder for this preprint (which was not certified by peer review) is the author/funder, who has granted bioRxiv a license to display the preprint in perpetuity. It is made available under aCC-BY 4.0 International license.

Figure S12. *In vivo* pull downs showing sAIM to cAIM conversion strengthening C53-ATG8 association and weakening C53-UFM1 association.

(A) Biological replicates of representative experiment shown in Figure5F. 6-day old *Arabidopsis* seedlings expressing AtC53-GFP, AtC53^{cAIM}-GFP in *c53* mutant background were incubated in liquid 1/2 MS medium with 1% sucrose supplemented with DMSO as control (Ctrl) or 10 μg/ml tunicamycin (Tm) for 16 hours and used for co-immunoprecipitation. Lysates were incubated with GFP-Trap Magnetic Agarose, input and bound proteins were detected by immunoblotting using the respective antibodies as indicated. **(B)** Quantification of blots in (Fig. 5F, Fig. S12A), UFM1 and ATG8 protein levels that associate with AtC53-GFP or AtC53^{cAIM}-GFP are shown. Bars represent the mean (± SD) of 3 biological replicates (BR).

bioRxiv preprint doi: https://doi.org/10.1101/2022.04.26.489478; this version posted April 26, 2022. The copyright holder for this preprint (which was not certified by peer review) is the author/funder, who has granted bioRxiv a license to display the preprint in perpetuity. It is made available under aCC-BY 4.0 International license.

Supplementary Data S1. Eukaryotic datasets used in the phylogenomic analysis. Species names, NCBI Taxonomy identifiers, genome assemblies, proteomes, and their sources for each species analyzed are provided.

Supplementary Data S2. Total number of beads, mean, median, standard deviation and p-values of the microscopy-based protein-protein interaction assays are reported.

Supplementary Data S3. Fiji macro and agarose bead model for automatic quantification.